13

Coupled Semiconductor Metal Oxide Nanocomposites: Types, Synthesis Conditions and Properties

Dr. Mohammad Reza Vaezi
Division of Nanotechnology and Advanced Materials,
Materials and Energy Research Center,
MERC, Karaj,
Iran

1. Introduction

A nanocomposite is a solid material containing two or more phases where one of the phases has the dimensions of less than 100 nanometers (nm), or structures having nano-scale repeat distances between the different phases that make up the material. One of the main types of nanocomposite materials is the coupled semiconductor metal oxides such as M_xO_y/ Me_zO_t (M and Me are referred to metal type and x, y, z, and t are the oxidation states in these metal oxides) which can be divided into four categories. The first is mixed oxide nanocomposite in which mixed oxides form solid solutions such as TiO_2/ SnO_2 nanocomposite. Into second category fall those mixed oxides that form distinct chemical compounds, such as $ZnCo_2O_4$ and $ZnSn_2O_4$. The third are systems that form neither compounds nor solid solutions such as TiO_2/WO_3 nanocomposite. Finally, there are those systems that form Core/ Shell nanocomposite structures.

These four categories of mixed oxide nanocomposites can be produced by several methods such as hydrothermal, chemical bath deposition, chemical vapor deposition, sol-gel and solid state techniques. Among the above- mentioned chemical methods that have been reported in literature, the most common ways for production of these nanosized coupled oxides are co-precipitation and hydrothermal methods. Recently, some of these nanosized coupled metal oxides are properly synthesized by the author and et- al and the studies have been focused on production, characterization and applications of these nanocomposites.

In this chapter, the principles, mechanism and experimental results of author's researches concerning to the synthesis of these nanosized coupled oxides (the above- mentioned four categories) such as ZnO/ TiO_2, ZnO/ SnO, ZnO/ Co_3O_4, Zn_2TiO_4 and $ZnTiO_3$ nanocomposites and ZnO/ Co_3O_4 and TiO_2/ SnO_2 core- shell nanocomposites by using the simple methods of co-precipitation and hydrothermall processes are reported. Due to the high specific surface area of the obtained powders, these nanosized coupled oxides have very good potential for applications in gas sensors, photo-catalysis and photo-electrochemical cells.

2. Mixed oxide nanocomposites which form distinct chemical compounds

2.1 Zn_2TiO_4 and $ZnTiO_3$ nanocomposites

Zinc titanates are promising candidates as dielectric materials [1-3]. It is reported that three compounds exist in ZnO-TiO_2 system, including Zn_2TiO_4 (cubic), $ZnTiO_3$ (hexagonal), and $Zn_2Ti_3O_8$ (cubic) [4-6]. Among these compounds, ilmenite-type hexagonal $ZnTiO_3$ compound has been reported to have superior electrical properties [3, 7, 8].

Li et al. [9] reported the formation of a new $ZnTiO_3$ (cubic) phase as precipitates inside the Zn_2TiO_4 matrix having the same structure and lattice parameter with Zn_2TiO_4 phase. Zinc orthotitanate, Zn_2TiO_4 can be prepared easily via the conventional solid-state reaction of $2ZnO.1TiO_2$.

One of the main procedures for producing the mixed oxides is to prepare the conditions for diffusion of oxides into each other [10, 11]. Due to dependence of diffusion coefficient of oxides on structure, surface area, etc., the crystallography and physical properties of the obtained particles can be changed by changing their morphology and particles size.

Although a large volume of literature is available on the synthesis of oxide nano- composite powder, very little attention has been given to the effect of synthesis conditions such as synthesis temperature on the morphology and particle size distribution of these nano-composites. Furthermore, no previous studies have been conducted on the influence of synthesis temperature on the diffusion processing of oxide particles (ZnO and TiO_2) into each other. It is interesting to know how the morphology and size distribution of obtained particles change with the variation of synthesis temperature. Therefore, the purpose of this paper is to present results of such studies for chemical bath deposited Zn_2TiO_4 and $ZnTiO_3$ nano- composites.

The nano-composites of crystalline ZnO with amorphous TiO_2 before calcination processing can be synthesized via chemical bath deposition, CBD. After calcinations, the nano-crystalline Zn_2TiO_4 and $ZnTiO_3$ from ZnO–TiO_2 (1:1 mol %) were prepared.

XRD patterns of ZnO-TiO_2 nano- composite powder without calcinations treatment are shown in Fig. 1. ZnO peaks were identified while amorphous TiO_2 particles were detected by XRF (Table 1) [12].

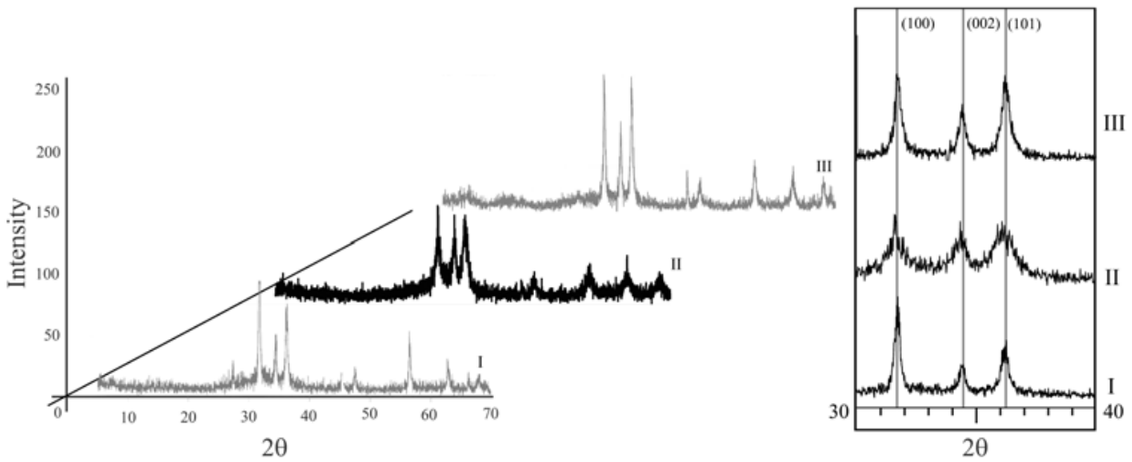

Fig. 1. XRD patterns of samples I (25 °C), II (45-50 °C) and III (70-75 °C) without calcinations [12].

Percentages of oxides(%wt)			Percentages of elements(%wt)				Samples
Other products	TiO_2	ZnO	Na	Cl	Ti	Zn	
18.1	39.7	42.2	5.3	14.1	30.2	48.6	Sample I
17.7	39.9	42.4	6.9	12.6	31.7	48.3	Sample II
20.4	34.8	44.8	6.2	10.2	31.3	51.2	Sample III

Table 1. XRF results of samples I, II and II [12].

With increasing the reaction temperature, the intensity of ZnO XRD peaks was increased. Also, with increasing the temperature, the sizes of obtained nano- particles was decreased and their morphologies tended to form semi spherical particles, which affected on the XRD peaks of obtained nano ZnO. This is well-agreed with reported observations of pure ZnO synthesis [12].

Based on the DTA of pure TiO_2 reported in the literatures [13, 14], the transformation from amorphous TiO_2 to crystalline TiO_2 is exothermic. Consequently, the temperature of 630 ˚C is selected for crystallization of amorphous TiO_2. All three samples were calcined for 4 hrs at cited temperature.

3.2 Formation of ZnO/$ZnTiO_3$/Zn_2TiO_4 nano- composite powders

Fig. 2 shows TGA/ DTA curves of the nano- composite powders produced by CBD method. As it can be seen, there is an undulating shape in the TGA curves (figures 2a, 2b, and 2c). The undulating shape of the TGA curves occurs in T > 350 ˚C. Also, a broad exothermic peak is clearly visible in the DTA curves close to temperature initialized the undulating behavior of TGA curves. The undulating shape of the TGA curves is caused by diffusion of the molecules of ZnO and TiO_2. Because of the diffusion of ZnO and TiO_2 phases, the compounds such as $ZnTiO_3$ and Zn_2TiO_4 may be formed. A broad exothermic peak observed at 350 ˚C <T < 600 ˚C in the DTA curves corresponds to atomic diffusion process occurred and therefore no considerable mass loss was detect in this region. A no sharp exothermic peak was also observed at ~ 630 ˚C in figures 2b and 2c. This peak corresponds to a phase transformation process of TiO_2 from amorphous to crystalline state.

After calcinations for 4hrs at 630˚C, XRD patterns indicate that ZnO coexists with $ZnTiO_3$, Zn_2TiO_4 and Ti_3O_5. In the XRD pattern of sample I synthesized at 25˚C, it can be detected $ZnTiO_3$ and Zn_2TiO_4 phases and the intensity of ZnO and Ti_3O_5 phases is negligible which can be ignored. It can be observed from these patterns that increasing the synthesis temperature decreases the amount of $ZnTiO_3$ and Zn_2TiO_4 phases and increases that of ZnO and Ti_3O_5 phases.

3. Mixed oxide nanocomposites which form neither compounds nor solid solutions

3.1 Synthesis of nanosized SnO/ZnO coupled oxides

Wang Cun et al reported the synthesis of ZnO/SnO_2 coupled oxides [15]. They compared the photocatalytic activity of ZnO/SnO_2 nano composites with their separate oxides. They observed that the photocatalytic activity of ZnO/SnO_2 nano composite was much more than SnO_2 and ZnO separately. They also proposed that its higher activity is because of lower recombination rate of electron-hole pairs in composite form. Similar results have been

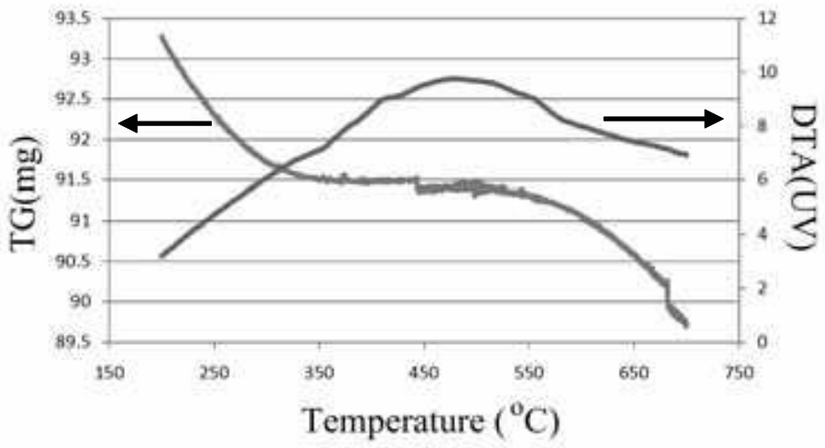

(a)

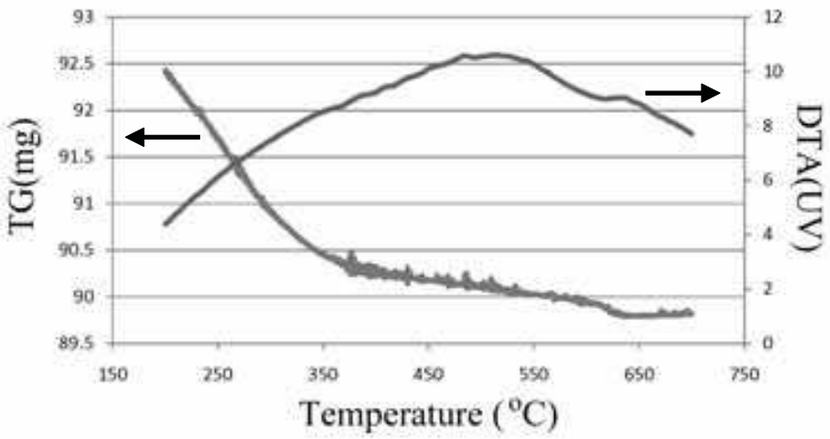

(b)

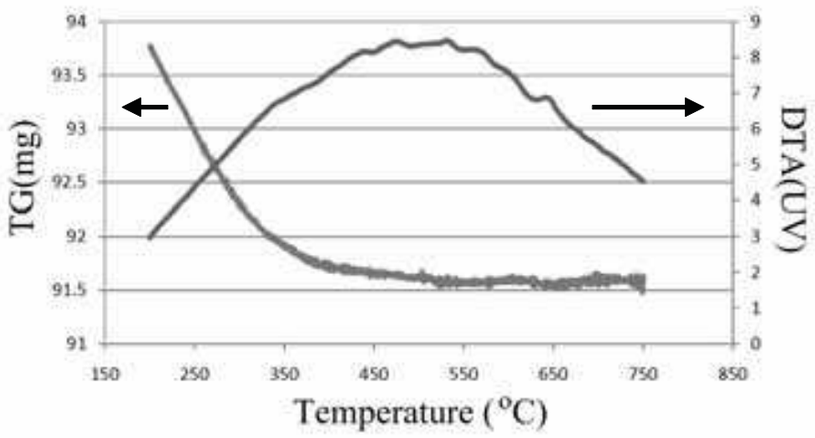

(c)

Fig. 2. TGA/ DTA curve of samples I (a), II (b), and III (c) [12].

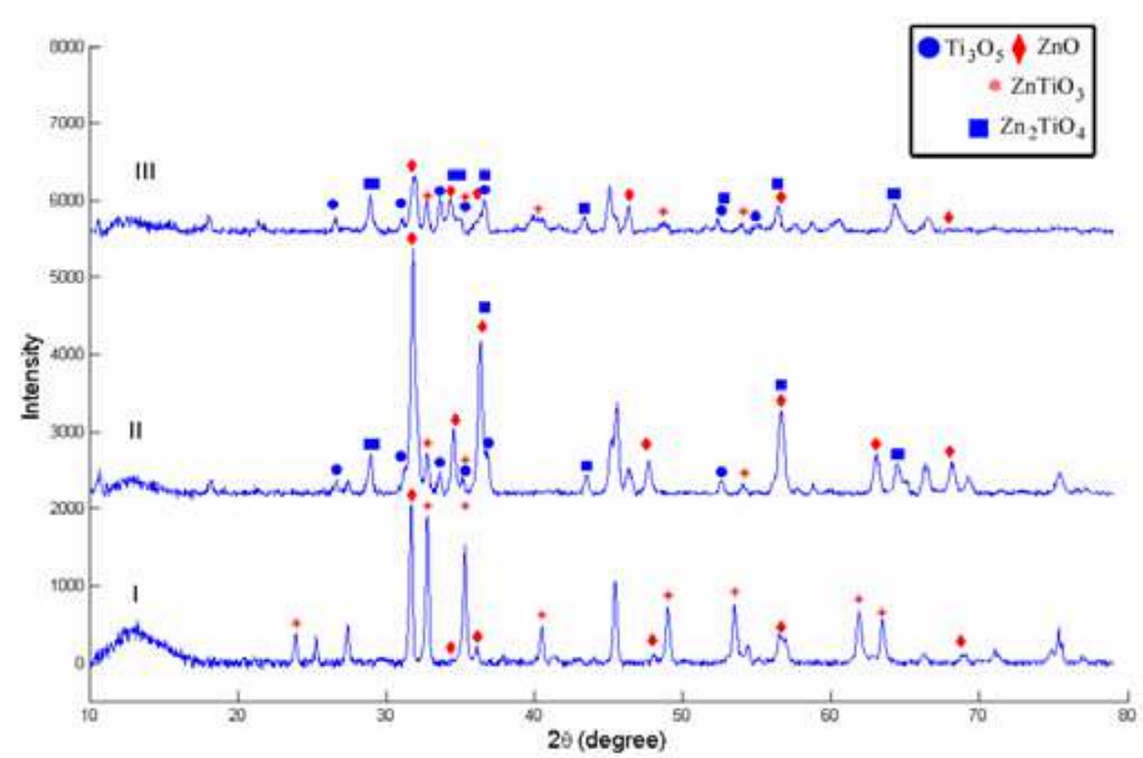

Fig. 3. XRD patterns of samples calcined at 630 ˚C (a) and the relative intensity of (101) peak for ZnO (b), (104) peak for $ZnTiO_3$ (c), and (211) peak for Zn_2TiO_4 (d) vs. the synthesis temperature [12].

reported in literature [16- 18]. Additionally Jinghong Li et al showed that by coupling nano oxides they usually show higher crystallinity and thermal stability, which can enhance their performance [18].

Recently, methods for obtaining nano- sized coupled SnO_2/ZnO are intensively developed and studies have been focused on production and characterization of these coupled oxides [16, 17, 19- 21].

A continual challenge for the researchers is to fabricate metal oxide materials, by controlling the oxidation state of multi valence metals ions in solutions. Although some studies have been conducted for production of nanosized SnO_2/ZnO coupled oxides, but the control of oxidation state of tin oxide in an aqueous solution in these coupled oxides has hardly been investigated.

Due to the fact that Sn(II) is easily oxidized to Sn(IV) , production of SnO/ZnO coupled nano oxide is relatively difficult. Thus, very few articles have been reported on the synthesizing of tin monoxide (SnO) [22-28] and to authors' best knowledge, no article on the synthesis of SnO/ZnO nanosized coupled oxide has been published till date.

In this section, fabrication of SnO/ZnO nanosized coupled oxide with oxidation state of II for tin in solution by using the simple method of co-precipitation is reported. These nanosized coupled oxides were obtained using $SnCl_2.H_2O$ and $ZnCl_2$ as precursors at three different temperatures. Due to the high specific surface area of the obtained powders, these nanosized coupled oxides have very good potential for applications in gas sensors, photo-catalysis and photo-electrochemical cells.

The procedure employed for preparing SnO/ZnO nano composites was as following: Two aqueous solutions of $SnCl_2$ and $ZnCl_2$ were added simultaneously dropwise to an aqueous solution of NaOH within about 30 min under vigorous stirring condition. This process was carried out at different temperatures of 25°C (sample I), 50°C (sample II) and 75°C (sample III) in beakers, each placed in a thermostatic cooling–heating water bath. Then the samples were kept for additional 2 hours under the same stirring condition and temperature. After synthesis, the powders were centrifuged and washed several times with distilled water and absolute ethanol and tested for removing of impurities specially NaCl with $AgNO_3$ and dried at 50°C in an oven.

The obtained phases are listed in Table 2. As shown in Table 2, final color of the synthesized sample at room temperature was pale yellow and the rest were dark green while becoming darker by increasing the temperature. During the synthesis of the sample I (at room temperature) the solution was always pale yellow, but for the other solutions after addition of certain amount of metal chloride solution that causes decrease in solutions pHs, the color of samples changed suddenly to dark green. It was observed that for sample III, this change in color occurred sooner than sample II. Also, by increasing the temperature from 25°C to 50°C the amount of the obtained powder increased drastically, as their initial solutions were the same.

sample	Synthesized temperature (°C)	Color	Obtained phases
I	25	Pale yellow	ZnO
II	50	Dark Green	SnO , ZnO
III	75	Dark Green	SnO , ZnO

Table 2. Condition of the synthesized powders

X-Ray diffraction patterns of the samples are shown in Fig.4. Brags peaks in sample I showed good agreement with ZnO (JCPDS no.36-1451), and no brag peaks of other compounds were found. But for the sample II and III the peaks are related to SnO (JCPDS no.06-0395) as well as ZnO (JCPDS no.36-1451).

Also, XRF analysis of sample I (Table 3) indicated existence of about 85.3 percent ZnO and 10.2 percent of SnO in the sample. Sn atoms can be doped in ZnO structure as two precursors of Zn and Sn are mixed together. As cited above, due to lack of SnO peaks in the XRD pattern of sample I, Sn should be formed as amorphous SnO or doped in ZnO during synthesis process. In fact this amount of doped Sn in comparison with the amount of Sn for Sample I is little enough to conclude that the major amount of Sn atoms have to be formed as individual amorphous phase instead of dopant in ZnO. J. Chouvin et al. reported synthesizing of SnO nano particles via CBD method. They used aquous solutions of $SnCl_2.2H_2O$ and NaOH as precursors of SnO and reported that by increasing temperature up to the boiling point, the mixtures' color turned from white to black and SnO crystals were formed during nucleation and growth of the previous amorphous phase [29]. This fact can be observed in this synthesis process too. The variation of obtained phase's ratio with increasing of synthesis temperature can be correlated to this phenomenon.

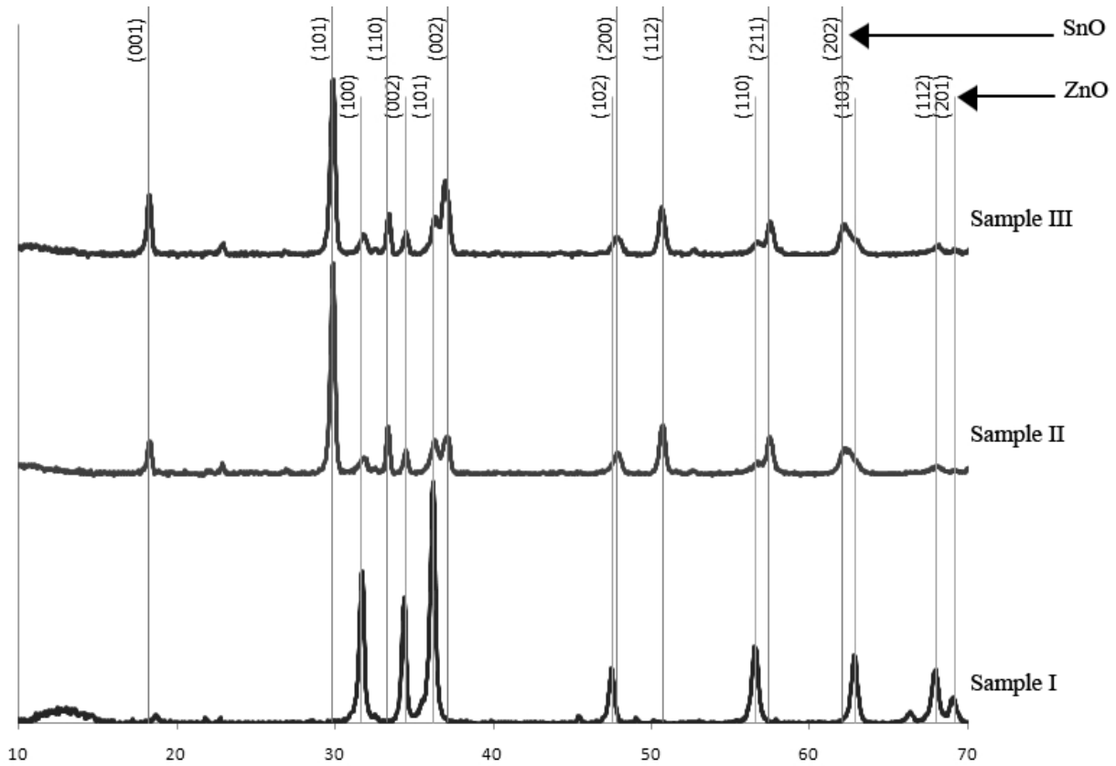

Fig. 4. X-Ray diffraction patterns of powders synthesized at 25 °C (sample I), 50 °C (sample II), and 75 °C (sample III).

Sample	Percentage of Products (%Wt)		
	ZnO	SnO	Other Products
I	85.3	10.2	4.5
II	48.2	48.6	3.2
III	51.7	45.6	2.7

Table 3. Results of XRF analysis of samples

The average crystallite size is calculated from the full width at half maximum (FWHM) of the diffraction peaks using the Debye–Scherer formula:

$$D = k\lambda / \beta \cos\theta \quad (1)$$

where D is the mean crystallite size; K is a grain shape dependent constant (here assumed to be 0.89); λ is the wavelength of the incident beam; θ is the Bragg reflection peak; and β is the full width at half maximum [30]. As can be seen in Table 4, the mean crystallite size of SnO particles from their (101) planes are 23.95 and 24.90 for 50 and 75°C, respectively. It can be seen from (002) plane of ZnO XRD patterns, at 25°C the mean crystal size of ZnO is about 23.56 nm but by increase in temperature to 50 and 75°C it decreased to 14.97 and 15.34 nm respectively. This decrease can be concluded from changing of obtained morphologies and growth conditions while increasing temperature [31, 32]. The results are listed in Table 4. Moreover the XRD results, at room temperature SnO wouldn't be formed, so the final pH of

this solution would be higher because of higher hydroxyl groups that remained in the solution. As existence of higher hydroxyl groups favors the growth of the crystalline phases; this condition favors the faster growth of ZnO crystals. As a result their crystallite sizes would be higher. Also it has been reported in literature that in this method, co-existence of seconds phase hinders the growth of crystals [33].

	ZnO		SnO	
sample	crystallite size (nm)	c/a	crystallite size (nm)	c/a
I	23.56	1.600	---	---
II	14.97	1.599	23.95	1.280
III	15.34	1.598	24.90	1.284

Table 4. Mean crystallite sizes and lattice constants of prepared samples

SEM images of samples are shown in Fig. 5. For particles of sample I, at the first glimpse it may look like that they are disc like particles but more precise investigation reveals that they are agglomerations of many tiny particles with 456.2 nm mean particle size. Mean particles sizes of samples are measured and listed in Table 5.

Sample	BET surface area (m^2g^{-1})	Mean aggregates size (nm)	Mean particle size (nm)
I	16.28	58 in width 260 in diagonal	45.2
II	22.88	58.4	34.4
III	19.84	52.4	36.5

Table 5. Specific surface area from BET, Mean aggregates size from SEM and mean particle size from TEM.

It was found that at 25°C, ZnO particles produce flake like agglomerates with median size of about 58 nm in width and 260 nm in diagonal as shown in Fig. 6a, but in fact this agglomerates are formed by smaller particles. At 50°C and 75°C the median sizes of obtained semispherical agglomerates of ZnO/SnO coupled oxides were 58.4 nm and 52.4 nm, respectively. From TEM images, these agglomerates as shown in Fig. 7, are formed from individual nanoparticles. The median sizes of obtained nanoparticles from TEM images and the agglomerates median sizes are listed in Table 5. As it can be seen, by change in temperature the sizes of obtained powders haven't changed intensively from sample II to III. But as listed in Table 5, due to enhancement in agglomeration, the specific surface area of the obtained samples are decreased by increasing synthesis temperature from 50 to 75°C.

The specific surface area of the obtained samples was calculated from Brunauer–Emmett–Teller (BET) equation and listed in Table 5. As it can be seen, BET surface area of obtained powders are 16.28, 22.88, 19.84 m^2g^{-1} for synthesized powders at 25, 50 and 75 °C, respectively. The lower surface area of sample I should be attributed to intense agglomeration of the particles in the form of plates. As mentioned above higher surface area of sample II is because of its lower agglomeration and also lower particle size.

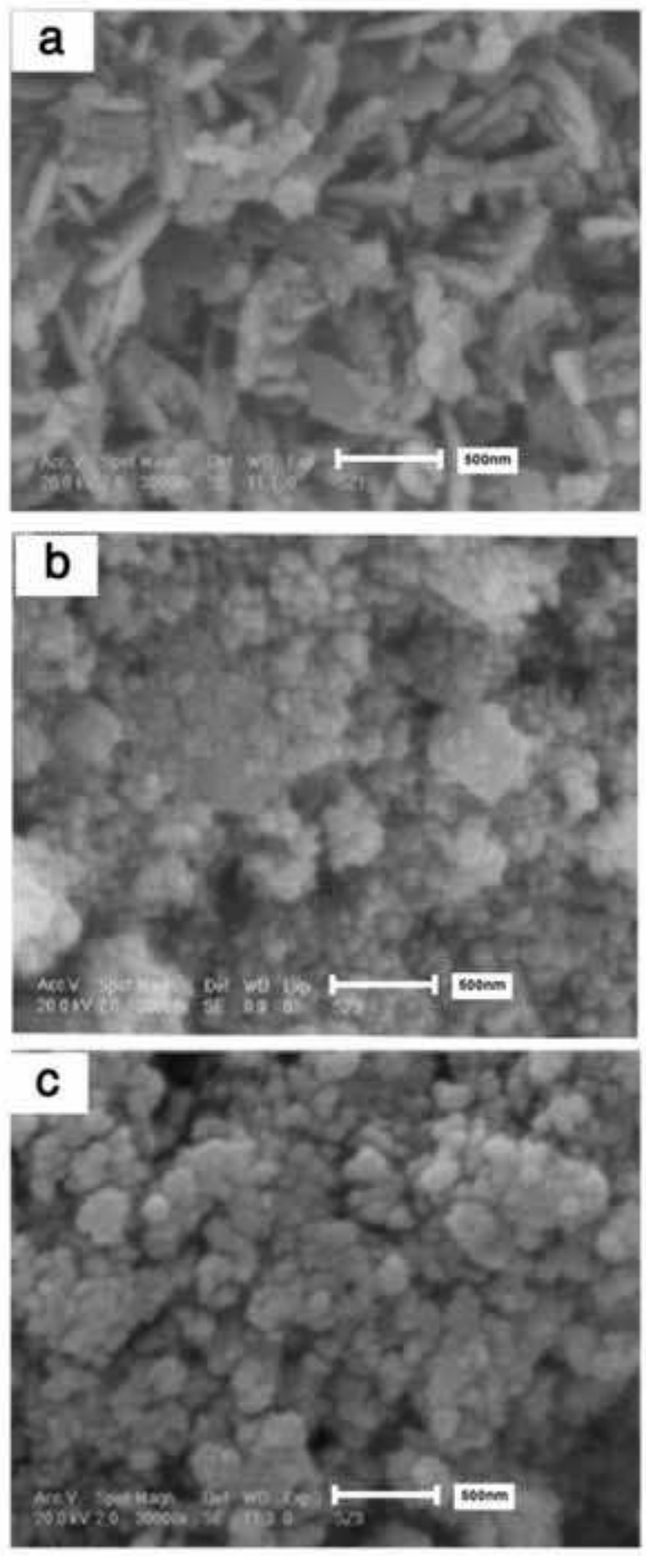

Fig. 5. SEM images of obtained powders at (a) 25, (b) 50 and (c) 75°C.

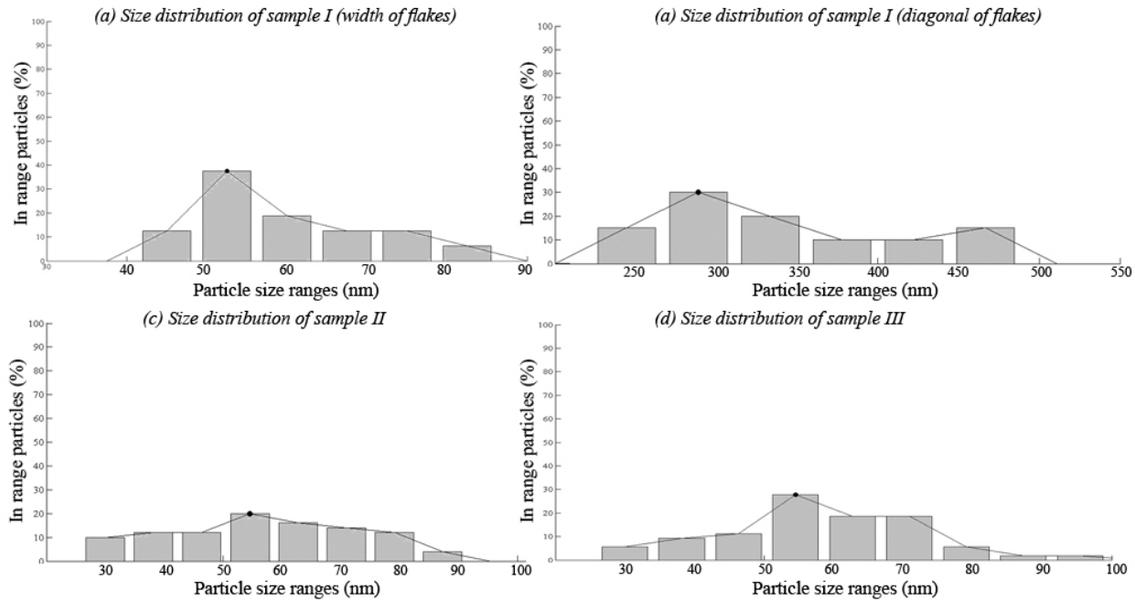

Fig. 6. Agglomerates size distribution of samples: (a) I (flakes width), (b) I (flakes diagonals), (c) II and (d) III.

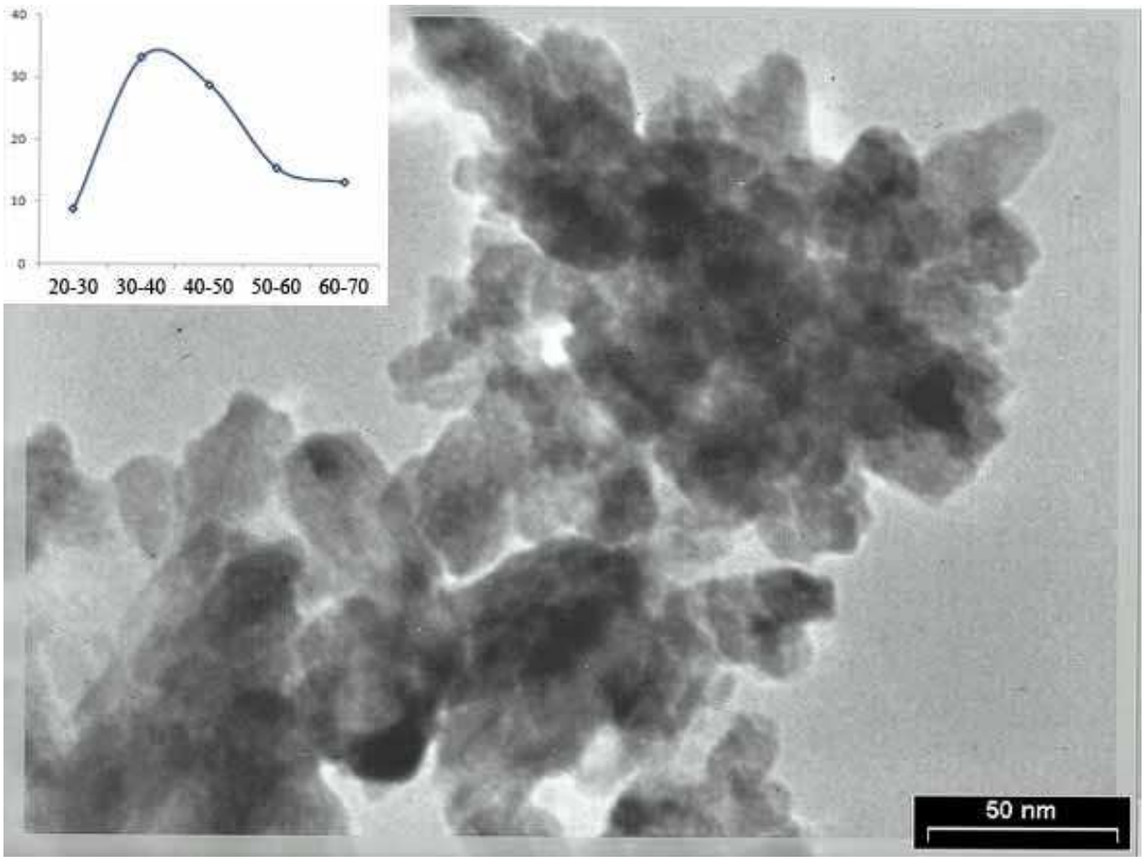

Fig. 7. TEM image of sample II with measured size distribution.

3.2 Synthesis of nanosized ZnO/Co_3O_4 coupled oxides via CBD method

Cobalt oxides are important materials that find applications in different fields such as catalysis, various type of sensor, electrochemical, electrical, and other opto-electronic devices [34]. Cobalt oxide is prepared by calcinations of $Co(OH)_2$ precursor synthesized by the chemical precipitation.

The main cobalt oxides are CoO and mixed Co(II) and Co(III) oxides ,Co_3O_4. When cobaltaus oxides are heated about 400-500 $^{\circ}C$ in oxygen, Co_3O_4 is readily obtained [35]. Co_3O_4 has typical spinel structure [36] and has various applications such as solid sensors, catalysts, electrode materials, magnetic materials, etc. In recent years, demands for monitoring of toxic and harmful gases have become more serious all over the world [37]. Various semiconductor gas sensors based on ZnO, SnO_2 and TiO_2 have been researched owing to their low costs and simple sensing method [38-40]. On the other hand, there still exist some disadvantages of them, for example, the poor sensitivity of SnO_2 [41] and high working temperature of ZnO [42]. In order to improve gas sensing properties of these sensors, many studies have been focused on novel metal catalysts such as Ag, Pt and Pd , materials doping, filming and oxides multiplicity (mixed oxides) [43] .

In this section, ZnO/ CoOH (before calcinations) and also ZnO/Co_3O_4 nanocomposites (after calcination at 300 $^{\circ}C$) were synthesized by CBD method at different synthesis temperatures.

Two separate aqueous solutions of Zn $(NO_3)_2.4H_2O$, KOH and $Co(NO)_3.6H_2O$ were prepared. $Zn(NO_3)_2.4H_2O$ and $Co(NO)_3.6H_2O$ solutions were added dropwise to KOH aqueous solution, simultaneously, within about 30 min ($\left[Zn^{2+}\right]/\left[OH^{-}\right]=1/2$ and $\left[Co^{2+}\right]/\left[OH^{-}\right]=1/2$) in a beaker under high stirring condition. After 30 minutes, the samples were kept for 2 hrs in the same operating conditions. The conditions used for synthesis of different samples are listed in Table 6.

The final samples were centrifuged and then, the precipitated products were washed with distilled water and absolute methanol several times. Finally, the precipitates were collected and dried at about 50 - 60 $^{\circ}C$ for 24 hrs. Also, the temperature of calcination was selected about 300 $^{\circ}C$ for all of the samples.

Sample	*Temperature °C*	*Stirring time (hrs)*
I	25-35	2.5
II	65-75	2.5
III	85-95	2.5

Table 6. Experimental conditions used for synthesis of nano- composite powders.

3.2.1 Synthesis before calcination

The results of XRD analysis of samples are shown in Fig. 8. In all samples, ZnO and $Co(OH)_2$ were detected. Comparing the patterns obtained from the samples, it can be seen that the peak intensities grow with increasing temperature. When the temperature was increased the intensity of $Co(OH)_2$ peaks became higher than that of ZnO peaks. The major

peaks can be noticed corresponding to (110) plane of ZnO for sample I and II whereas in sample III major peak is related to (101) plane of $Co(OH)_2$. Also, the intensity of peaks related to ZnO is grown by increasing the temperature.

Esmaielzadeh and his co-workers found that the morphology of ZnO converted from flake state to nano particles. They reported that, via increasing the temperature, the particle size decreased and the intensity of ZnO peaks increased too. We can detect this fact in the pattern of ZnO- $Co(OH)_2$ nano- composites [44] .

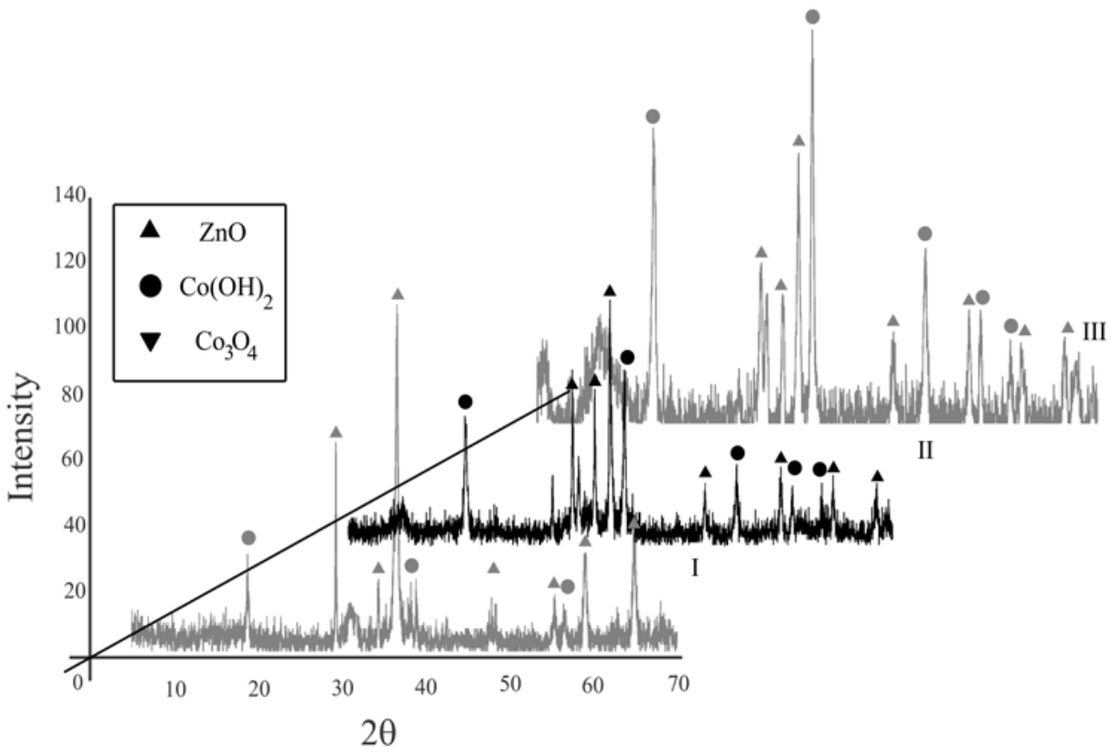

Fig. 8. XRD patterns of samples I, II, and III before calcinations.

The SEM images of the samples are shown in Fig. 9. The effect of synthesis temperature can be detected from these images. The SEM micrographs clearly indicate that the nano-composite samples are composed of spherical and semi- spherical nano- particles as well as flake shaped crystallites at ambient temperature. Also, from SEM images (Fig. 9) the maximum, minimum and median sizes with respect to samples size distributions can be obtained from the image processing program programmed with visual C++. The size distributions of samples I, II and III as well as the particle size ranges obtained from changing the synthesis temperatures are illustrated in Fig. 10.

The maximum, minimum and median sizes of obtained samples are shown in Table 7.

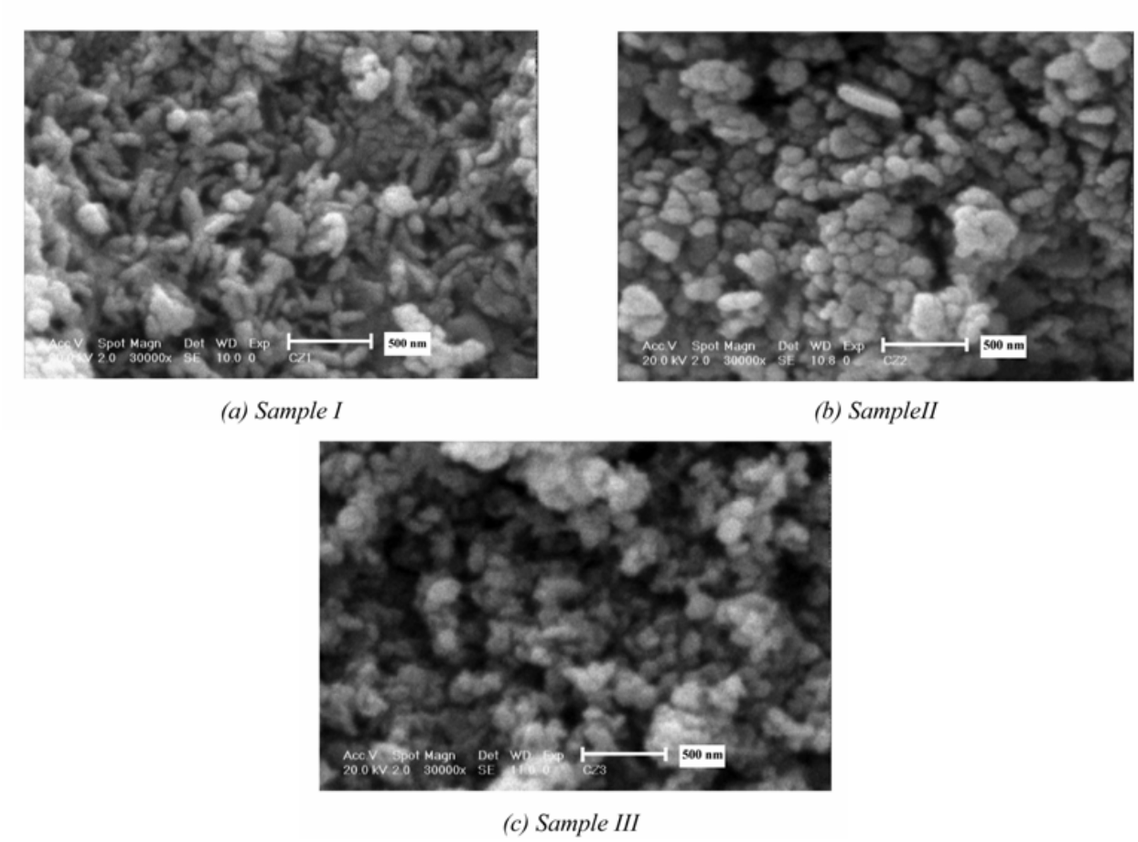

Fig. 9. SEM images of samples synthesized at (a) 25-35 °C (b) 65-75 °C (c) 85-95 °C .

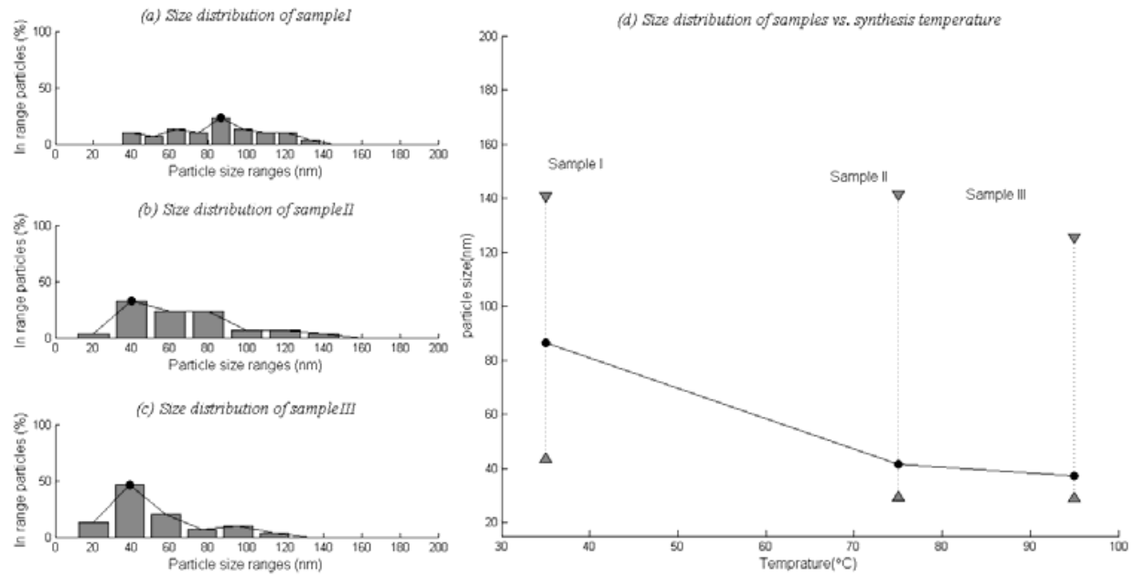

Fig. 10. Histogram of particle size distribution of (a) sample I, (b) sample II, (c) sample III and (d) The effect of synthesis temperature on the spherical particle's diameters for samples I, II and III. The particles size ranges are indicated as vertical bars on the figure.

Sample	*Synthesis temperature °C*	*Maximum particle size (nm)*	*Minimum particle size (nm)*	*Median particle size (nm)*
I	25-35	140	43	86.67
II	65-75	41	29	41.52
III	85-95	125	28	37.21

Table 7. Maximum, minimum and median sizes of samples I, II and III.

3.2.2 Synthesis after Calcination at 300 °C

From other investigations about converting $Co(OH)_2$ to Co_3O_4, DTA analysis indicated that $Co(OH)_2$ converts to Co_3O_4 at about 280 °C [45]. Moreover, no peaks of pure ZnO (exothermic or endothermic) were shown in DTA curve at 280 °C indicating no exothermic or endothermic transformations occurred at this temperature.

The thermal behaviors of obtained samples were carried out at argon atmosphere. Fig. 11 illustrates thermal behavior of sample I. In all of these analysis, because of coexistence of ZnO beside of $Co(OH)_2$, the distinct $Co(OH)_2$ peaks which had been detected in other papers would not detected here. But an endothermic tiny peak has been detected at about 284 °C (see Fig. 11).

Consequently, all of three samples calcinated for about 4 hrs at 300 °C in air atmosphere. The results of XRD analysis of samples are shown in Fig. 12.

The SEM images of nano- composite powders I, II and III calcinated at 300 °C are shown in Fig. 13. As can be seen, calcinations processing causes eliminating the flakes and the calcinated nano- composite samples are predominantly composed of spherical and semi-spherical nano- particles. Also, from SEM images presented in Fig. 13 the maximum, minimum, median sizes with respect to particle size distributions can be obtained from image analyzing process. The results can be seen in Fig.14 where the vertical lines are particle size ranges.

The maximum, minimum and median sizes of obtained samples are shown in Table 8.

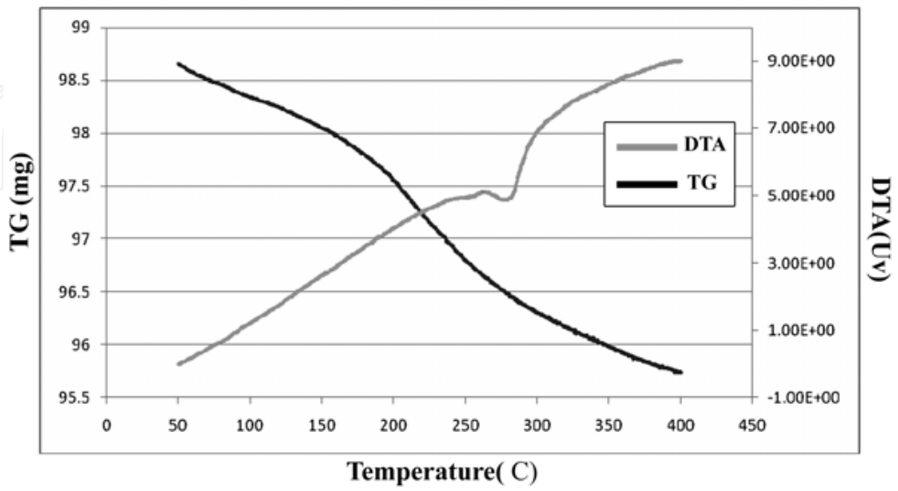

Fig. 11. DTA/ TGA analysis of sample I.

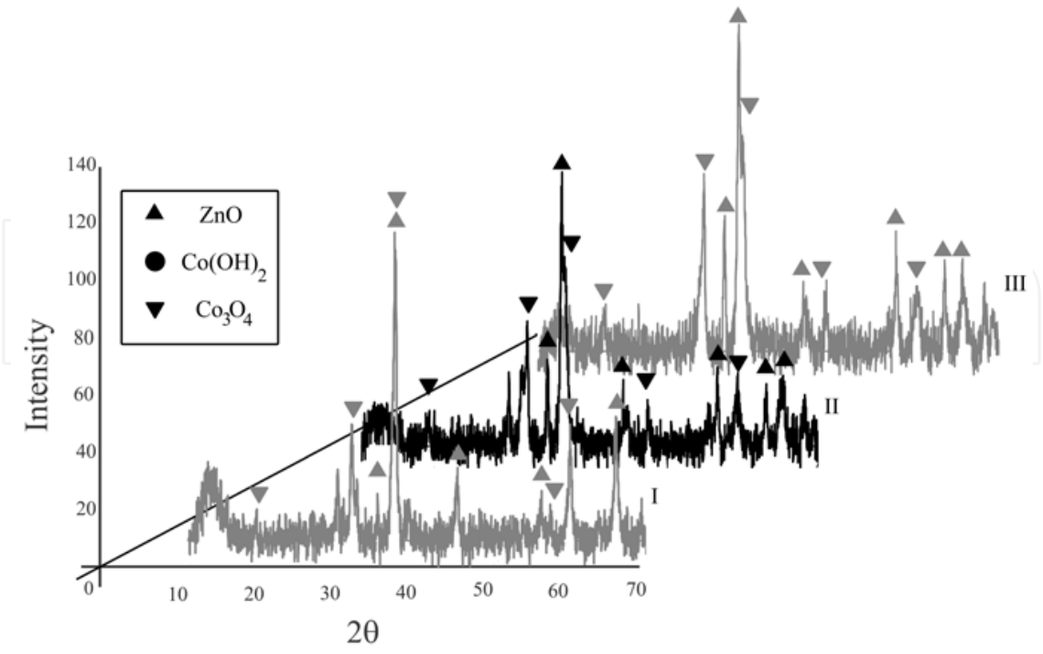

Fig. 12. XRD patterns of samples I, II and III after calcination in 300 °C for 4 hrs at air atmosphere.

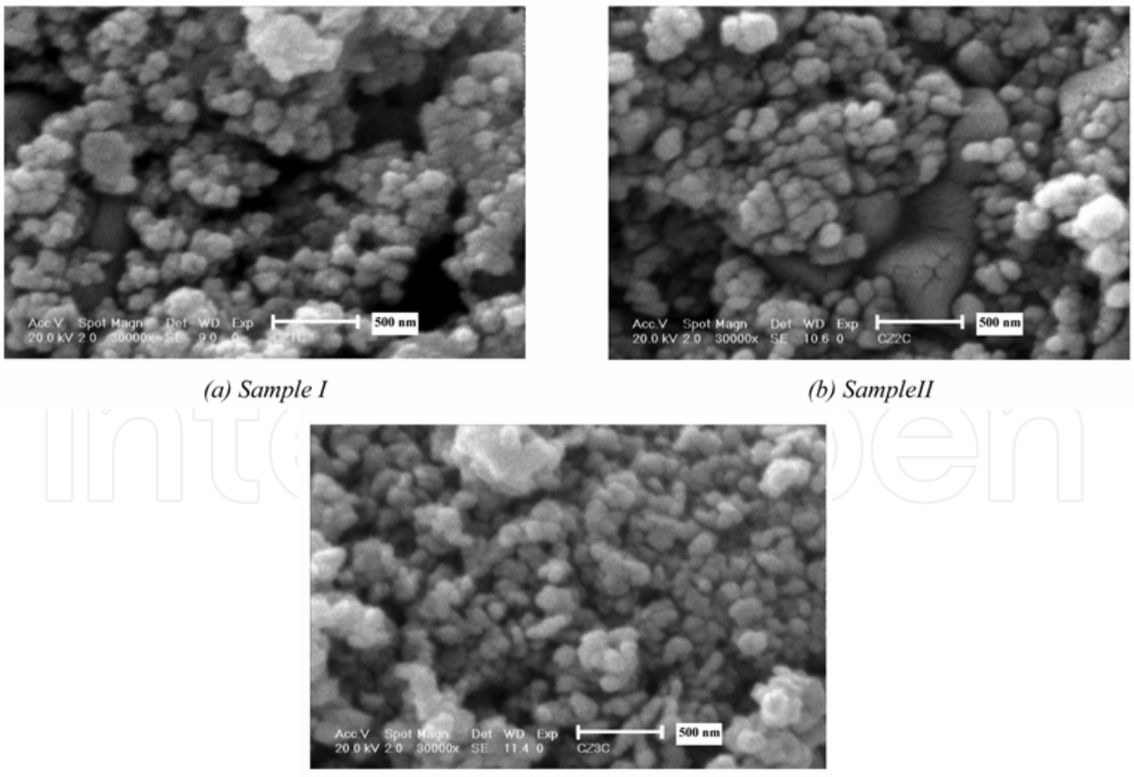

(a) Sample I

(b) SampleII

(c) Sample III

Fig. 13. SEM images of samples (a) I, (b) II and (c) III after calcinations.

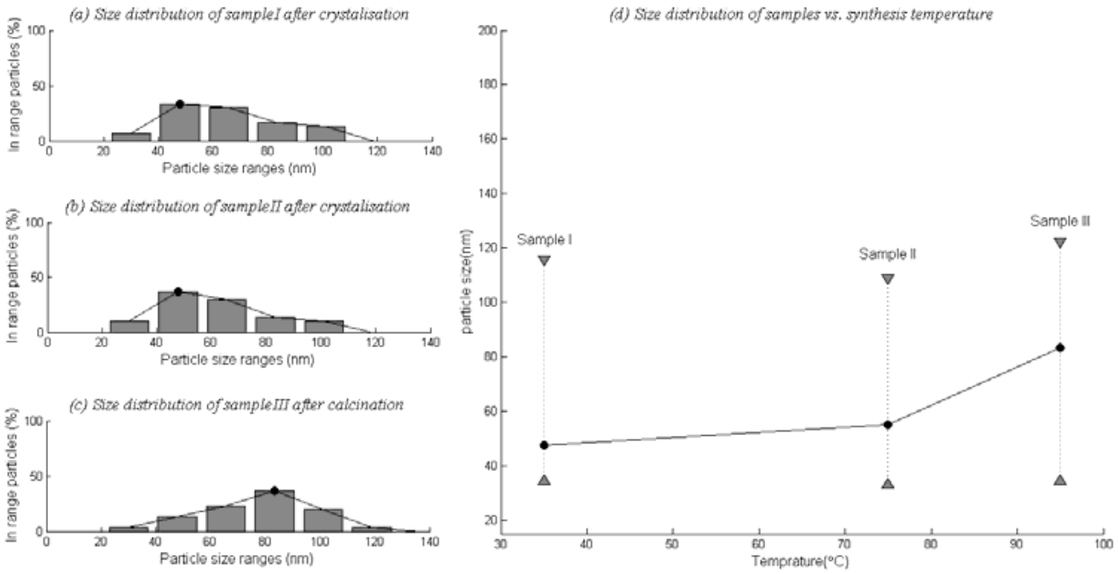

Fig. 14. Histogram of particle size distribution of (a) sample I, (b) sample II, (c) sample III after calcination and (d) The effect of synthesis temperature on the spherical particle's diameters for samples I, II and III after calcination. The particles size ranges are indicated as vertical bars on the figure.

Sample	*Synthesis temperature °C*	*Maximum particle size (nm)*	*Minimum particle size (nm)*	*Median particle size (nm)*
I	25-35	115	34	47.8
II	65-75	150	33	55.3
III	85-95	130	34	83.33

Table 8. Maximum, minimum and median sizes of samples I, II and III after calcinations.

3.3 Synthesis of nanosized ZnO/$Co(OH)_2$ coupled oxides via hydrothermal method

Recently, lamellar materials have been widely researched; layered hydroxide materials have attracted much interest in the production of catalyst, sorbent, ionic exchangers, ionic conductors, and electrochemical materials [46]. β-Cobalt hydroxide, has recently received increasing attention due to its application in the electric, magnetic and catalytic materials [47]. The atomic arrangement of $Co(OH)_2$ represents a member of the brucite type structure family (space group: $P\bar{3}ml$, point symmetry $\bar{3}2ml$). The cobalt hydroxide has hexagonal layered structure in which a divalent metal cation is located in an octahedral site generated by six hydroxyl oxygen atoms [48].

Three different theories were reported for studying the growth behaviour of materials. The BFDH law starting from planar mesh density, and considering the effects of screw axis and glide plane on crystal growth habit, provides a predicted theoretical growth habit of the crystal [49]. The PBC theory provides an ideal growth habit of crystals in terms of bond chain types between molecules and attachment energy [50]. But the above mentioned models have some shortages in explaining or predicting the crystal growth habit. The Growth Unit Model is based on the individual units which they contribute in the growth

procedure. This theory hypothesizes that in the crystallization stage of oxides, cations exist in the form of complexes with OH^- ligands which their coordination numbers are equal to those of the crystal formed. These complexes are called growth units. W. Zhong was the first to put forward the Growth Unit Model [51] and nowadays many investigations were carried out by considering this theory for describing the growth behavior of the different materials [52].

The effects of surfactants on the morphologies produced in hydrothermal synthesis of different compounds were studied extremely [53-55]. The surfactants can be divided into two major categories including ionic and non-ionic surfactants. These surfactants affect the morphologies of the synthesized nanoparticles. In fact for the reaction system in the presence of surfactants, the surface tension of solution is reduced due to the existence of surfactant, which reduces the energy needed for the formation of a new solid phase [56].

CTAB is a well known cationic surfactant which can be ionized completely in water. The structure of this surfactant is shown in Fig. 15(a) [57].

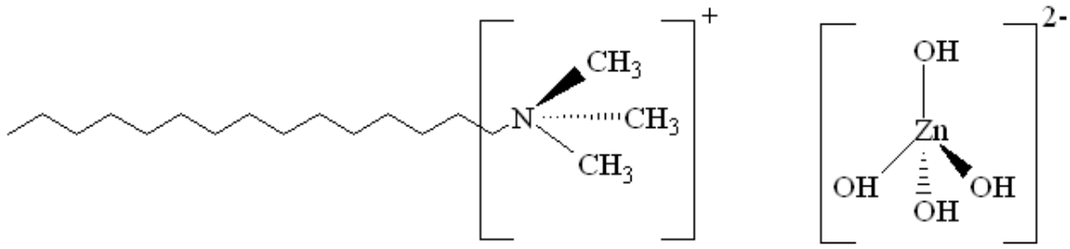

Fig. 15. The structure of (a) CTAB and (b) $Zn(OH)_4^{2-}$

In this section, ZnO/ $Co(OH)_2$ nano-composites were synthesized by hydrothermal method at 160 °C for different synthesis periods. CTAB was used as ionic surfactant.

Three separate aqueous solutions of $Zn(NO_3)_2.4H_2O$, KOH and $Co(NO_3)_2.6H_2O$ were prepared. $Zn(NO_3)_2.4H_2O$ and $Co(NO_3)_2.6H_2O$ solutions were added to KOH aqueous solution simultaneously under high stirring conditions. After mixing, the obtained solution was divided into 4 portions and poured to separate beakers. Then the surfactants were added to beakers while the solutions were being stirred with high intensity. After 5 minutes, the solutions were poured into a 35 mL Teflon-lined autoclave with a filling capacity of about 80%, then sealed and maintained at appropriate temperature for different periods. The conditions of synthesis are shown in Table 9. The prepared samples were filtered and washed with distilled water and absolute methanol several times. Then samples were dried at 60 °C for 24 hrs.

Sample	Surfactant		Time (hrs)
	Type	Amount (g)	
I	---	---	5
II	CTAB	0.1	5
III	---	---	24
IV	CTAB	0.1	24

Table 9. Synthesis conditions.

XRD patterns of samples I, II and III are shown in Fig. 16. From these patterns, $Co(OH)_2$ and ZnO were detected. From XRD patterns and SEM images (Fig. 17), the effect of surfactant on

XRD patterns and the obtained morphologies can be understood. In sample I, the absence of surfactant causes producing sharper XRD peaks, but the surfactant in other samples affects the growth conditions and thereby particle sizes and morphologies, so the sharpness of the peaks in sample II is different to sample I.

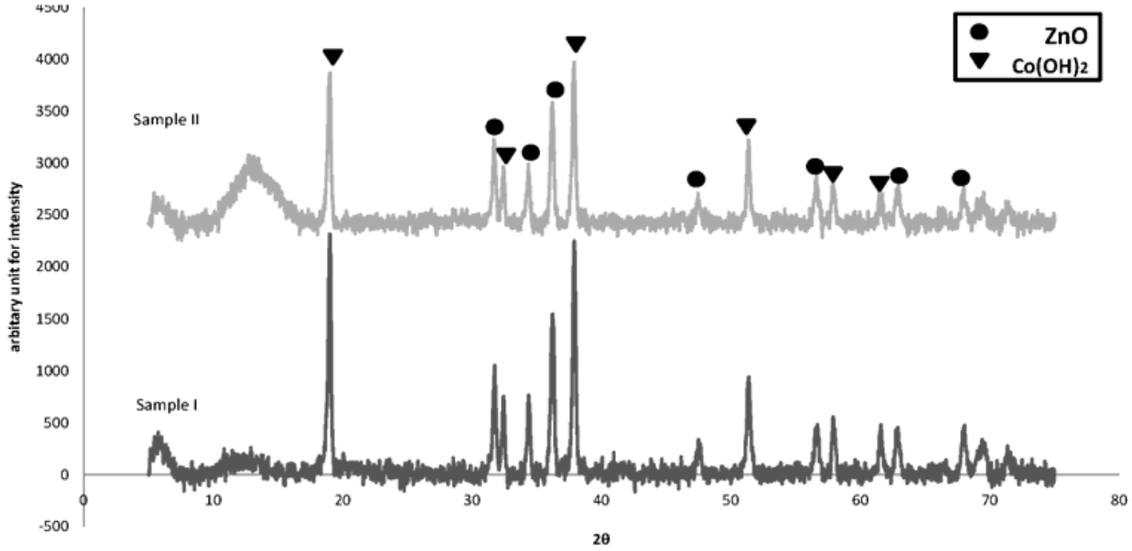

Fig. 16. (a) XRD patterns of samples I and II.

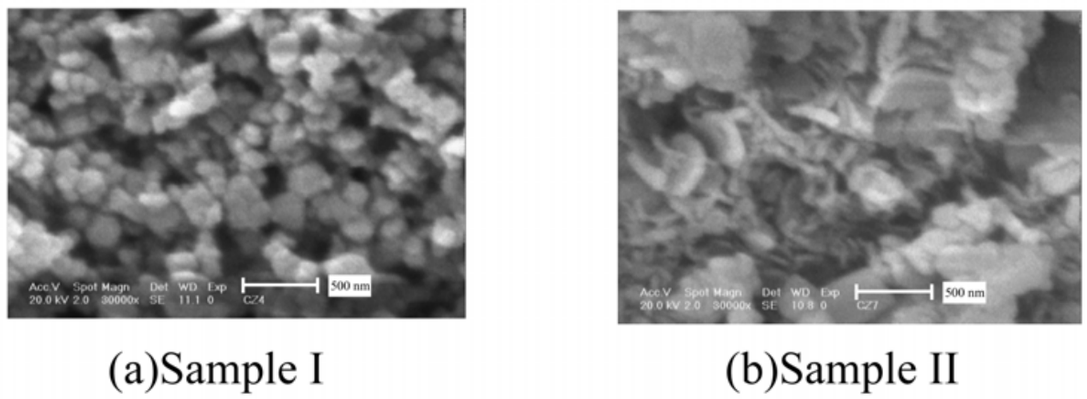

Fig. 17. SEM images of samples synthesized for 5 hrs at 160 °C

From SEM images and XRD patterns, the intensity of the peaks can be contributed to the type of morphologies obtained. For example, by comparing sample I to sample II, the morphologies were converted from semi spherical to needle like morphologies, due to presence of CTAB as a surfactant, and the intensities of XRD peaks were differed too.

For other samples synthesized for 24 hrs, the XRD patterns are shown in Fig. 18. Same as samples I and II the XRD patterns with and without CTAB are different. Also, the intensity of peaks is different like the previous samples and this can be related to size distribution and type of morphology. SEM images of samples III and IV are shown in Fig. 19.

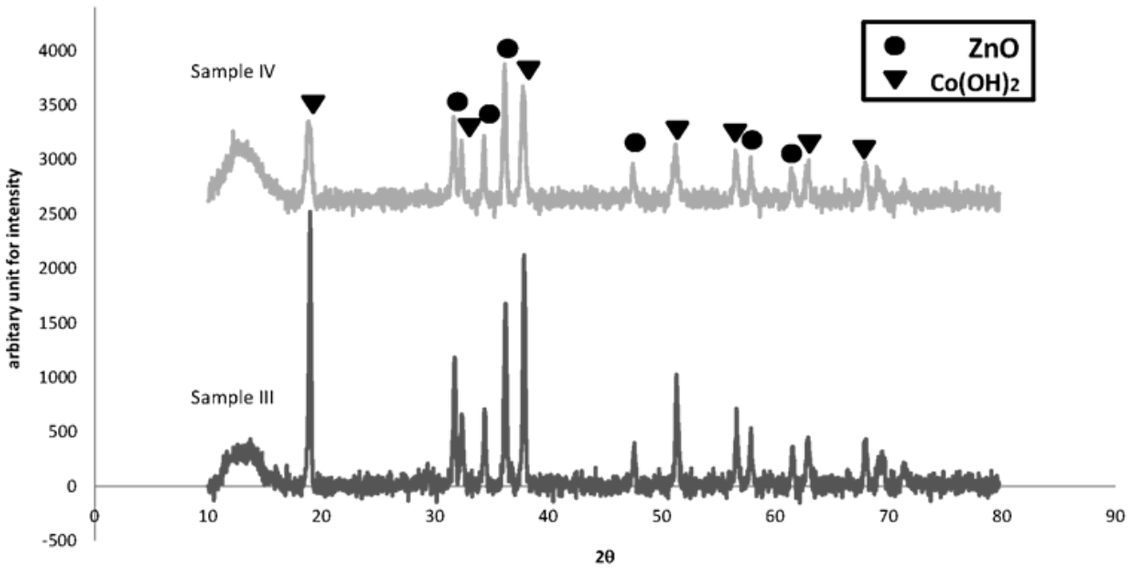

Fig. 18. XRD patterns of samples III and IV.

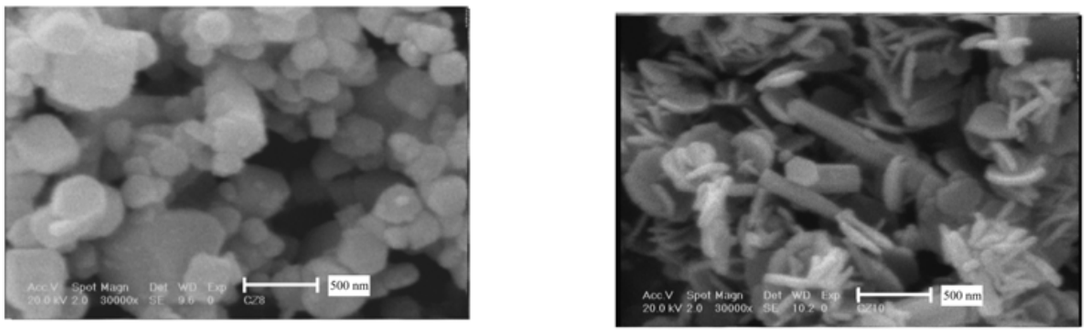

(a)Sample III (b)Sample IV

Fig. 19. SEM images of samples synthesized for 24 hrs at 160 °C

By comparing Fig. 18 to Fig. 19, the effect of periods of hydrothermal synthesis on the morphology and growth rates can be detected. As it can be seen, in presence of CTAB, the growth rate of samples II and IV is reduced in comparison with samples I and III.
The results of median sizes and crystallite size of samples are listed in Table 10.

Sample	ZnO plane	Mean Crystallite Size (nm)	$Co(OH)_2$ plane	Mean Crystallite Size (nm)
I	(101)	24	(101)	29
II	(101)	23	(101)	21
III	(101)	33	(101)	32
IV	(101)	27	(101)	23

Table 10. The mean crystallite sizes of the samples.

3.3.1 Synthesis of ZnO without surfactants

The main efforts have been carried out on hydrothermal synthesis of ZnO nanoparticles by Wen-Jun Li et al. [58]. They synthesized ZnO from $Zn(AC)_2$ and Na(OH) precursors at 200-300°C by hydrothermal method and conclude from the IR and Raman analyses that the growth units of ZnO are Zn complexes with OH^- ligands in the form of $Zn(OH)_4^{2-}$. The main reactions in forming ZnO can be divided into four stages, including:
Stage I) Ionization of zinc salts and sodium hydroxide in water:

$$Zn(M)_2 \xleftrightarrow{ionization} Zn^{2+} + 2(OH)^- \tag{2}$$

$$Na(OH) \xleftrightarrow{ionization} Na^+ + (OH)^- \tag{3}$$

Where M represents negatively charged groups of Zinc salts.
Stage II) Precipitation of Zinc hydroxide:

$$Zn^{2+} + 2(OH)^- \xrightarrow{solved\ in\ water} Zn(OH)_2 \downarrow \tag{4}$$

Stage III) Formation of $Zn(OH)_4^{2-}$ in hydrothermal conditions:

$$Zn(OH)_2 + 3(OH)^{2-} \xrightarrow{hydrothermal} Zn(OH)_4^{2-} \tag{5}$$

Stage IV) dehydration of $Zn(OH)_4^{2-}$ complexes:

$$x(Zn(OH)_4^{2-}) \xrightarrow[hydrothermal]{dehydration\ durring} (Zn_xO_y(OH)_z^{(x+2y-2x)-}) + (x-1)H_2O \tag{6}$$

Where, the x, y and z represent the numbers of Zn^{2+}, O^{2-} *and* OH^- respectively.
Therefore, the oxide particles can be produced by stacking of these complex polyhedrons by sharing their elements. In the interior parts, the oxygen ions are the connection centers where the exterior and the surface of the particles are $(OH)^-$ ligands, which have been proved by IR [59, 60] and Raman [61, 62] spectra in other investigations. So in the complex of $(Zn_xO_y(OH)_z^{(x+2y-2x)-})$, $(OH)^-$. ligands exist in the interface of the crystal while the interior parts consist of ZnO units as shown in Fig. 20. So stacking of these crystallites in hydrothermal condition can produce nanostructures [58]. Existence of Cobalt ions during this process can affect the morphologies and can be doped in the ZnO structures too [63].

3.3.2 Synthesis of $Co(OH)_2$ in hydrothermal processing

The formation mechanism of $Co(OH)_2$ is different to that of ZnO. When Cobalt salt is dissolved in water, it is ionized to Co^{2+} and M^- (where M represents negatively charged groups of Cobalt salts) and the first and second stages are same as ZnO, as is shown in equations (7) to (9).
Stage I) Ionization of Cobalt salts and Sodium hydroxide in water:

$$Co(M)_2 \xleftrightarrow{ionization} Co^{2+} + 2M^- \tag{7}$$

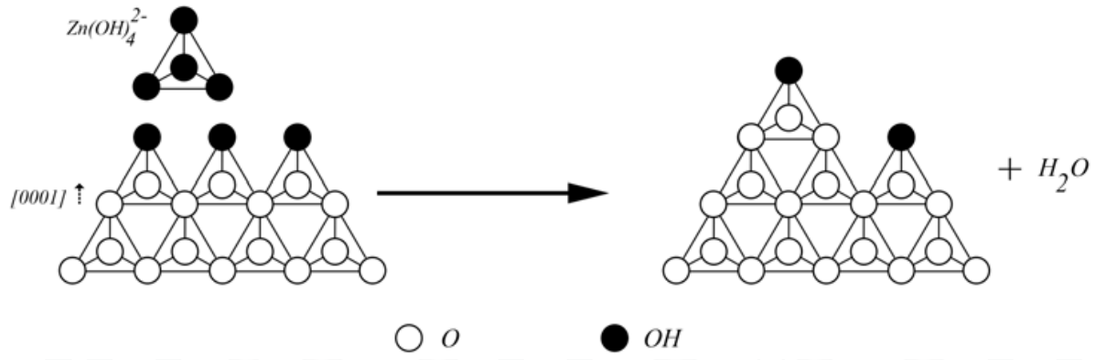

Fig. 20. Idealized interface structure image of ZnO crystal in [0001] direction and the Growth Unit Mechanism of crystallization of ZnO.

$$Na(OH) \xleftrightarrow{ionization} Na^{+} + (OH)^{-} \tag{8}$$

Stage II) Production of Cobaltous hydroxide:

$$Co^{2+} + 2(OH)^{-} \xrightarrow{solved\ in\ water} Co(OH)_2 \downarrow \tag{9}$$

B. Basavalingu et al. investigated the transformation of $Co(OH)_2$ to Cobalt oxides by hydrothermal synthesis. They calculated the minimum pressure and temperature for formation of CoO from $Co(OH)_2$. The calculated values are in good agreement with experimental data [64].
The saturated pressure of water in 160°C can be calculated from Antoine equation [65]:

$$\log P = A - \frac{B}{C + T} \tag{10}$$

Where A, B and C are 8.07131, 1730.63 and 233.426, respectively.
At 160°C, the pressure calculated from equation (10) is about 2.98144 bars, while for formation of CoO in this temperature higher pressure is necessary. The pressure for this transformation is higher than 500 bars. So by considering growth unit model and thermodynamics of formation of cobalt oxide from $Co(OH)_2$, the growth units of cobalt oxide do not form at 160°C and 3 bar pressure. So the nanoparticles of $Co(OH)_2$ grow by gathering the crystallites of $Co(OH)_2$.

3.3.3 Growth in the presence of CTAB

The effects of CTAB on the final morphology in the hydrothermal synthesis have been investigated extremely [53, 65]. After ionization in water, CTAB produces a cationic structure with a positively charged tetrahedron and a long hydrophobic tail. This tetrahedron is positively charged and can act as a cationic surfactant and affect the final structure of synthesized particles due to its electrostatic forces and stereochemical effects. The complimentary between CTA^{+} and $Zn(OH)_4^{2-}$ (Fig. 15) endows the surfactant the capability to act as an ionic carrier [59]. As it is shown in Fig. 20, due to presence of OH^{-} ligands on $(Zn_xO_y(OH)_z^{(x+2y-2x)-})$ surface in the hydrothermal processing, a negatively charged film forms on its surface when CTA^{+} which has a good complimentary with

$Zn(OH)_4^{2-}$ attract on its surface and a networks of CTA+ forms on $(Zn_xO_y(OH)_z^{(x+2y-2x)-})$ surface. When the surfactant molecules leave, zincate will be carried away in the form of ion-pairs, so that the barrier layer becomes thinner (as shown in Fig. 21), and forms a rod-like morphology [53]. These phenomena can become more effective after CMC point of CTAB [57].

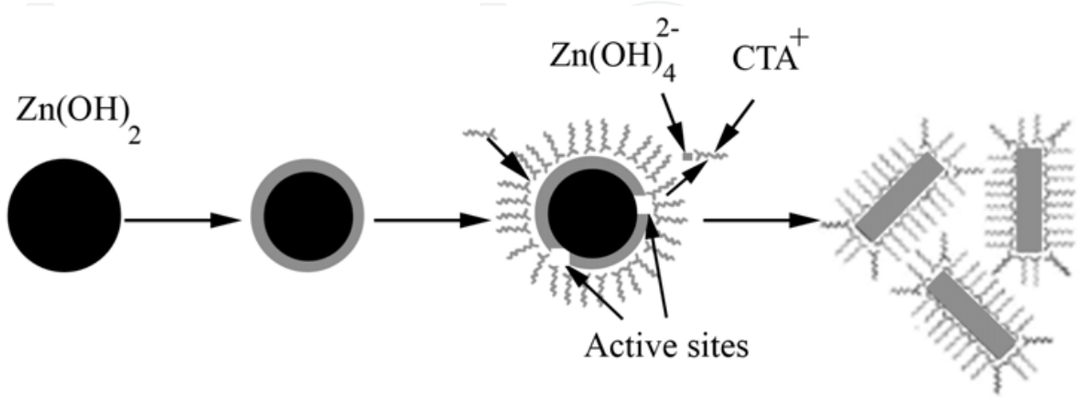

Fig. 21. Schematic illustration of the erosion process in the presence of CTAB. Black color, $Zn(OH)_2$, gray color, $Zn(OH)_4^{2-}$. The wave -like patterns indicates the CTA+ ions. A CTA+ ion carrying a zincate ion is shown.

In the crystallization process, surfactant molecules may serve as a growth controller, as well as an agglomeration inhibitor, by forming a covering film on the newly formed ZnO crystals. This can be resulted not only from absorption of CTA^+ on the surface of zinc complexes but also the stereochemical effect of its hydrophobic tail.

Due to thermodynamically limits for formation of growth units of cobalt oxide, as cited before, CTAB absorption on cobalt ions is restricted. The main effect of CTAB on the morphologies of $Co(OH)_2$ can be deduce from the stereochemical effects of surfactants which gathered on adjacent Zinc complex surfaces and also the repulsion of CTA^+ and Co^+ which restrict the in-situ ion concentrations of Co^+ and Zn^+.

Thus as shown in Fig. 17 and 19 the morphology of nano-composite consists of ZnO nano-rods and $Co(OH)_2$ nano-hexagonals.

4. Core/ Shell nanocomposite

4.1 TiO_2/ SnO_2 core/ shell nanocomposites

Recently, a lot of interest in core– shell nanocomposites has arisen due to their advantages such as stability, high catalytic activity, controllable compositions and structure, and so on [66,67]. In the coupled semiconductor systems, two different NPs are in contact and thus holes and electrons could be accessible on different particle surfaces, if needed for selective oxidation and reduction processes. In the core/shell geometry, a shell layer is coated onto the core particles and only one of the charge carriers is available at the surface of the shell for redox reaction and the other one is trapped inside (see Fig. 22) [68].

In this section, TiO_2/ SnO_2 core shell nanocomposites were produced via sol- gel method and the ethanol sensing behavior of the TiO_2/ SnO_2 nanocomposites was investigated and compared with the pure TiO_2 nanoparticles.

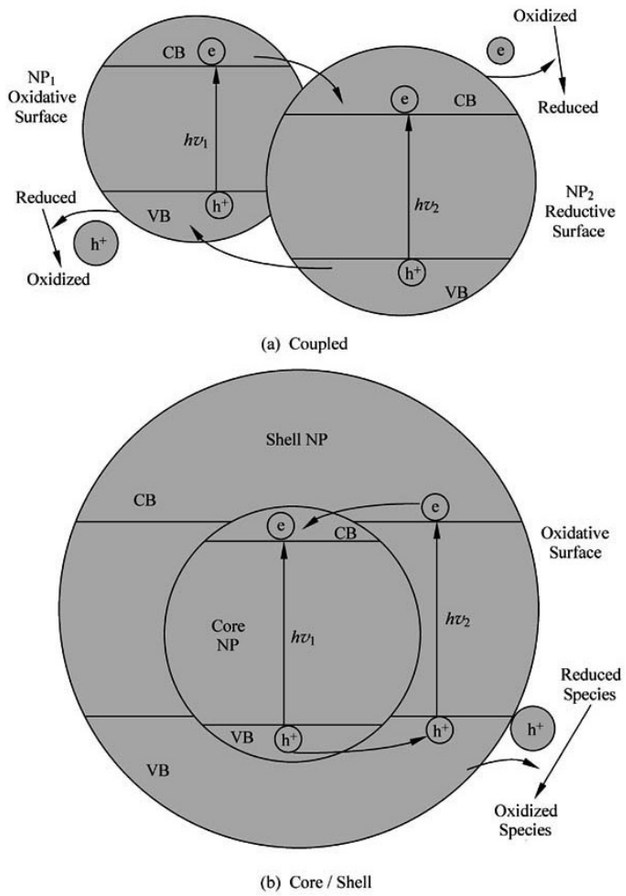

Fig. 22. Schematics of photoinduced charge separation and subsequent interfacial redox processes in (a) coupled and (b) core/shell geometry of semiconductor NPs [68].

All the chemical reagents used in this study are of analytical grade and used without any purification and treatment. TiO_2 nanoparticles were prepared from initial aqueous Ti^{4+} stock solution and hydrothermal treatment. The initial solutions were obtained by adding of 5.4 ml of titanium isopropoxide (TTIP) and same amount of isopropanol to 56.6 ml of distilled water at pH 1.5 achieved by an acid. TTIP solution was maintained under stirring conditions for a day at room temperature. Certain amount of triethylamine (TEA) was then added dropwise to solution containing Ti till pH value reached 7. It has been reported that the use of amines could act as shape controller template [69]. The obtained solution was then poured into a 35 ml Teflon lined stainless steel autoclave up to 70 vol% and maintained at 120 °C for 12 h. The autoclave was then cooled naturally to room temperature. TiO_2 powders were obtained by centrifugation and 3 times washing with distilled water. Thus, the obtained precipitates were then filtered and dried at 120 ˚C for 12 h.

The coating of SnO_2 nanoparticles on TiO_2 nanoparticles (core shell nanocomposite) was performed at room temperature by the following process:

0.2 gr. titania nanoparticles obtained were dispersed in a solution of NH_4OH and de-ionized water. Then, $SnCl_4.5H_2O$ diluted with de- ionized water was poured into the above-mentioned solution and hereby a white slurry was produced. After stirring 24 h., the resulting product was filtered and dried at 60 ˚C. The various molar proportions of Ti to Sn

were examined. The symbol of TS1-1, TS1- 1.5 and TS1-2 are denoted as core shell nanoparticles based on the molar ratio of Ti to Sn 1:1, 1:1.5 and 1:2, respectively. All as-synthesized samples were calcined as 500 ˚C for 1 h.

Fig. 23 shows the SEM image and ED analysis of TiO_2/ SnO_2 nanocomposite with molar ratio 1:2. As it can be seen, the composite nanoparticles are spherical particles and have homogeneous morphology.

Also, according to Fig. 23 (b), the presence of Ti, Sn and Au atoms can be confirmed. Au atoms correspond to coating of Au on the particles surface.

The TEM micrographs of typically TiO_2/ SnO_2 nanoparticles are shown in Fig. 24. It can be clearly seen from the micrographs that a SnO_2 coating is on the TiO_2 surface forming core shell structure of TiO_2/ SnO_2 nanoparticles. The particle size in TiO_2/ SnO_2 nanocomposite sample TS1-2 is greater than that of TS1-1. ED pattern (Fig. 24c) shows diffuse rings, indicating the formed TiO_2/ SnO_2 is polycrystalline.

A certain amount of nanocomposite powder was pressed to form a disk with diameter of 1 cm. and thickness of 1mm. Then, the obtained sample sintered at 500 ˚C for 1 h. was considered as sensing element. The details of construction and schematic illustration of the fabricated gas sensor has been reported in the reference [70].

The responses of all sensors to ethanol have been measured at different concentrations ranging from 500 to 5000 ppm and at operating temperature in the range from 140 to 420 ˚C to investigate the gas sensing properties. Fig. 25 shows the sensor responses to ethanol for TiO_2 and nanocomposite samples at various operating temperatures.

Working temperature is one of the most important parameters for gas sensors. The conventional gas sensors based on SnO_2 and TiO_2 materials operate at the temperature region from 300 to 400 ˚C [71], but the response of sensors based on TiO_2/ SnO_2 nanocomposite to 1000 ppm ethanol was at around 200 ˚C. For the molar ratios of 1:1.5 (TS1-1.5) and 1:2 (TS1-2), the responses to 1000 ppm ethanol were 3.2 and 2.95, respectively. Meanwhile, at lower concentration of SnO_2 (TS1-1), there was no response. This observation can't be clearly explained yet and is under investigation by authors.

The dependence of the response on ethanol concentration at optimum operating temperature is shown in Fig. 26. It can be seen that nanocomposite sensors present more sensitivity than TiO_2 sensor at the concentration range from 500 to 5000 ppm ethanol. TS1-1.5 sample indicates the best sensitivity than the others. It was found that the response and recovery times of the sensors are less than 50 s.

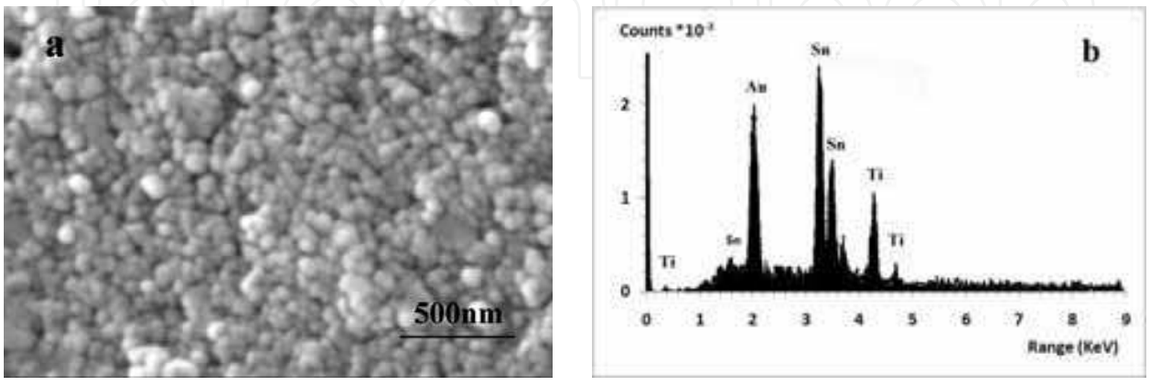

Fig. 23. a) SEM image and b) SEM- EDS element analysis of sample TS1-2.

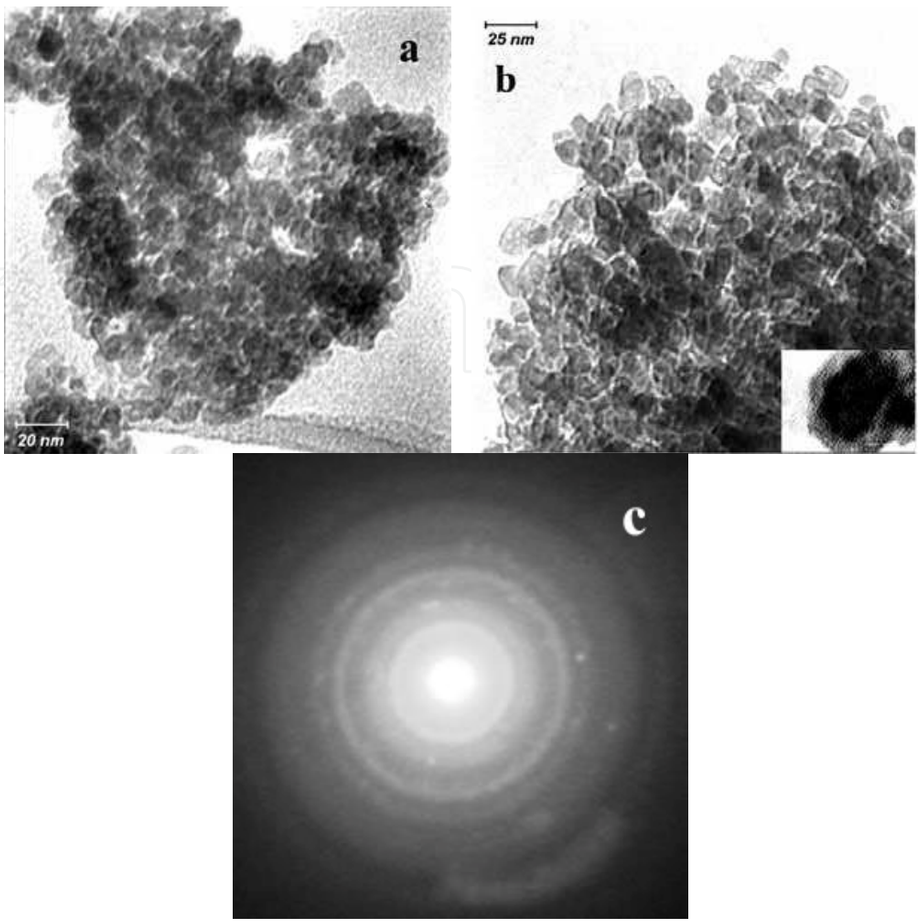

Fig. 24. TEM micrographs of TiO_2/ SnO_2 nanoparticles samples (a) TS1-1 and b) TS1-2 together with ED ring pattern of TiO_2/ SnO_2 nanoparticles.

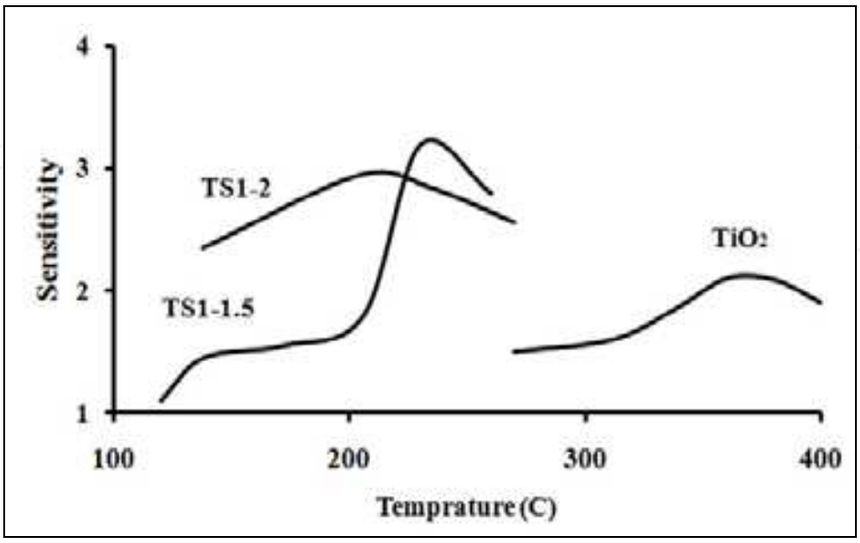

Fig. 25. The dependence of response on operating temperature for TiO_2, TS1-1.5 and TS1-2 samples.

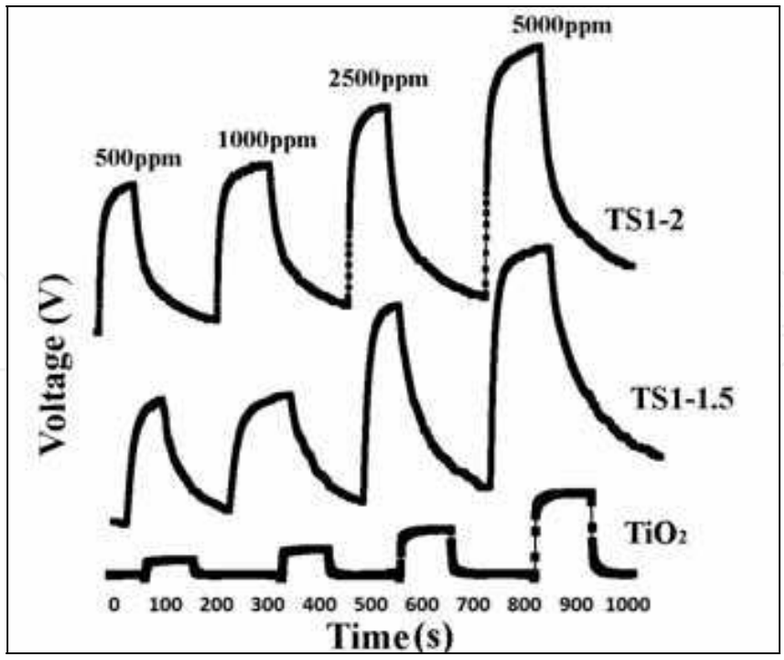

Fig. 26. The dependence of the response on ethanol concentration at optimum operating temperature.

4.2 Co_3O_4/ZnO Core/Shell nanoparticles

By emerging nano-materials a tremendous effort has been carrying out for investigating on their significant properties which make progressive improvements in many scientific fields. Among these nano-materials, nano-semiconductor materials have become one of the major fields in which attentions of different researchers, from bioscience to optoelectronics, have been attracted due to unique properties of these nanoparticles and dependency of their final properties on the size of particles. Nano-photocatalysts are one of the well known subroutine categories of semiconductors' applications. Their advanced and vast applications including cancer treatment, purification and sterilization of water and air, self cleaning coatings, etc make them one of the most important nano materials for daily uses.

Cancer is the top cause of the death in the world wide. Conventional methods for cancer treatments, surgical, radiological, immunological, thermo-therapeutic, and chemo-therapeutic treatments are well-known. The first attempts for cancer treatment by photocatalysts are related to A. Fujishima et al. efforts, in which TiO_2 nanoparticles were injected in the cancer tumors and exposed to high intensities of light. The results indicated on the fact that nano-photocatalysts can inhibit the tumor growth. Also, high ratio of surface to volume in nanoparticles causes the surface reactions occur better by contributing of major numbers of consisting molecules of a particle in surface reactions. Regardless the considerable benefits of nano-drugs, the side effects of nano material usage are considerable. The inability in controlling drug delivery endangers healthy cells on chemical toxicity. Thus, nowadays production of well controllable delivery systems has been increasing among researchers.

In environmental applications, un-purified water which contains considerable amounts of photocatalysts could become a problem. By exposing light to the remained photocatalysts,

for each photon an electron-hole pair produces and subsequently it degrades the adjacent media. Due to unselective manner of aforementioned phenomenon, harmful and useful cells both are attracted with produced electron-hole pairs. The conventional methods for separating nano-particles from the media have low efficiency as well as high costs. Also, two major properties should be considered while using photocatalysts: specific surface area and band gap energy of prepared photocatalysts. High amount of specific surface area is one of the main functional variables for adsorbing cells on particles surface and increasing the active sites for photocatalytic reactions. On the other hand, most of the photocatalytic properties of semiconductors are related to their optical band gap. These properties show the workability of a photocatalyst.

Core/shell nanocomposites are one of the solutions for many difficulties in which a bifunctional nano-architecture or a modification in properties, which can't be achieved by using one type of nano-particles, is needed. Using a magnetic core enables directing particle using safe external magnetic field. If a core/shell composite contains magnetic core and semiconductor shell with high surface area and proper photocatalytic properties, the delivery and also purification of the particles become possible.

Co_3O_4 is a well known magnetic p-type semiconductor material. The performance of tri-cobalt tetra-oxide particles is highly dependent on the nanoparticles size and their specific surface areas. Thus, many attempts have been done to synthesize Co_3O_4 with high specific surface area and low dimension, such as sol-gel, chemical bath deposition (CBD), chemical vapor deposition (CVD) and hydrothermal methods. Among these, hydrothermal processing is widely used due to production of fine and uniform structures with high controllability in growth and also it can be used for preparation of fine and uniform nano Co_3O_4 particles.

Zinc oxide (ZnO) is one of the most important semiconductors. This material in nano scale shows specific properties which make it applicable as promising photocatalysts, light emitting diode, sterilization, etc. Many different chemical approaches have been reported for synthesizing ZnO nanoparticles such as hydrothermal, sonochemical, sol-gel, etc. Among these synthetic routes, sol-gel is known as one of the main synthesis routes for applying homogenous films on different surfaces and particles and thus, it is one of the main and important routes for making core/shell hetero-structures.

In this section, a promising route for synthesizing Co_3O_4/ZnO core/shell via soft chemical route has been reported. H_2O_2- assisted hydrothermal method was used for synthesizing Co_3O_4 core nanoparticles, while ZnO shell was obtained via sol-gel method.

4.2.1 Core nanoparticles

NH_4OH aqueous solution (pH=10) with appropriate amount of H_2O_2 were added drop by drop to $Co(Ac)_2$ aqueous solution in 30 minutes. The obtained solution was poured into 90 ml Teflon lined autoclaves and filled up to 80% of its volume. Then, the autoclaves were kept at 180 °C for 24 hours. After that, the autoclaves were cooled to room temperature naturally, and precipitates were filtered and washed with distilled water and ethanol for several times. Finally, the obtained powders were dried at 50 °C for 24 hours. The procedures are shown in Fig. 27.

4.2.2 Core/shell nanoparticles

A simple sol-gel procedure was used for producing ZnO shells on the Co_3O_4 nanoparticles. 0.3 g Co_3O_4 was dispersed in 50 ml solution of pure methanol and TEA with weight ratio of

$\left[\frac{TEA}{Zn(Ac)_2}=1\right]$. Another solution prepared by dissolving $Zn(Ac)_2$ in 50 ml deionised water. The concentration of $Zn(Ac)_2$ in final solution was 0.3 M. Both solutions were sonicated for 30 min. then, the second solution poured into the first solution under stirring condition and was kept for 2 hours at 60 °C. The obtained core/shell particles were filtered and dried at 50 °C for 24 hours. Then, the dried powder was calcined for 2 hours at 400 °C. The schematic diagram of procedure is shown in Fig. 28.

XRD patterns of synthesized nanoparticles are shown in Fig. 3. As it can be seen from Fig. 29, the peaks are attributed to Co_3O_4 (JCPDF 42-1467) for core nanoparticles and no other peak is detected while in core/shell just some undetectable traces can be detected from core nanoparticles. In core/shell nanoparticles, all major peaks are contributed to wurtzite ZnO (JCPDF 36-1451). The main reason for fading core particles in the XRD pattern of core/shell can be related to considerable amounts of ZnO nanoparticles synthesized adjacent to core nanoparticles. If thickness of produced shell films on the surface of the core particles were

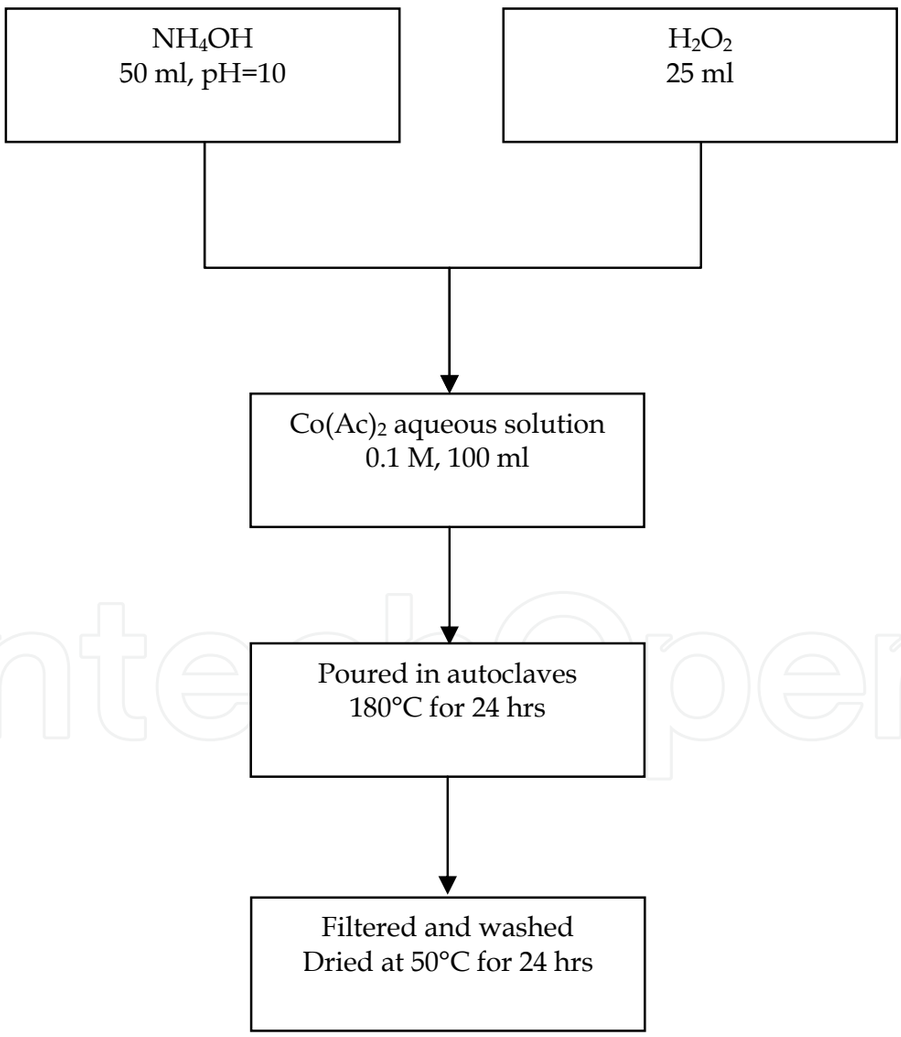

Fig. 27. Flowchart for synthesizing Co_3O_4 nanoparticles.

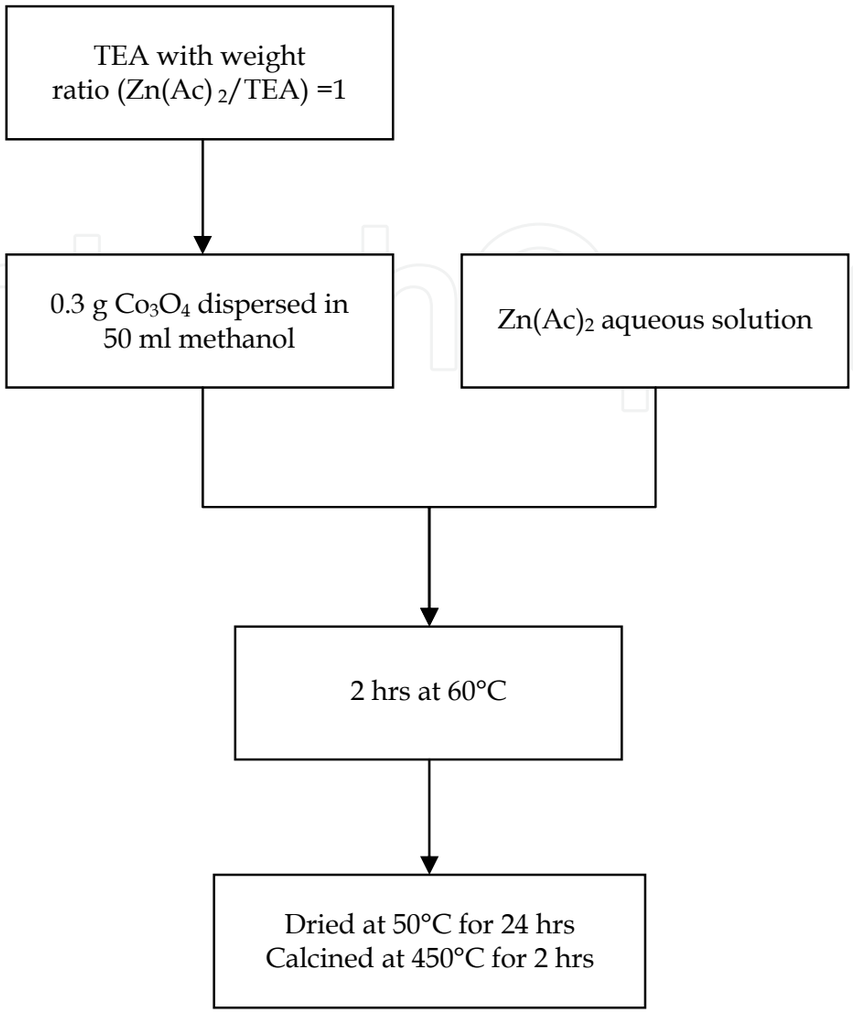

Fig. 28. Flowchart for synthesizing Co_3O_4/ZnO nanoparticles.

considerable in comparison with core nanoparticles, a reduction in the intensity of core peaks can be detected. Also, if the mass fraction of produced shell was much more than used core nanoparticles, it could result in reduction of core peaks in XRD patterns. The mentioned phenomena can intensify reduction in peaks intensities of core nanoparticles and also increase the noises in the core/shell patterns.

TEM images for the obtained core and core/shell nanoparticles are shown in Fig. 30. It can be seen that the median particle size of Co_3O_4 is about 22 nm where in core/shell nanoparticles, existence of the shell around the core particles makes the particles bigger and thus the median particle size is about 56 nm. Also, the darker parts of the image (Fig. 30b) in core/shell are related to core where brighter ones are related to ZnO shells. From BET analysis, the specific surface areas for core and core/shell were detected 98.6 and 54.6 m^2/g, respectively. BET adsorption isotherms for core and core/shell are shown in Fig. 31. The plotted isotherms represent highly isotherm of Type III. It has been shown, if a solid contains no porosity, its isotherm tends to appears as a Type III isotherm. Also, decrease in the specific surface area could be another reason for formation and growth of ZnO shells on Co_3O_4 surface and subsequence decrease in specific surface area.

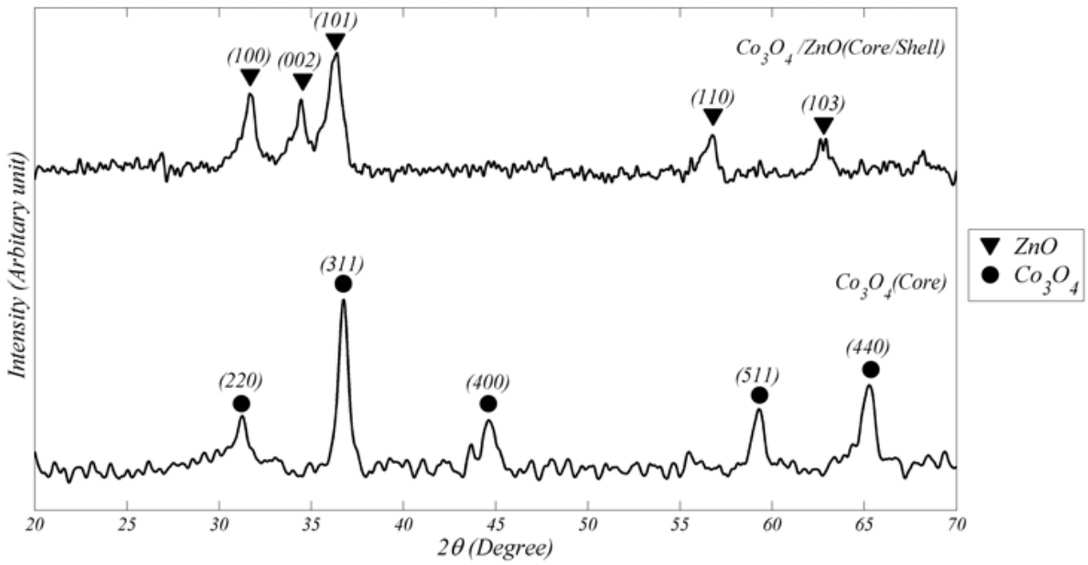

Fig. 29. XRD patterns of core and core/shell nanoparticles.

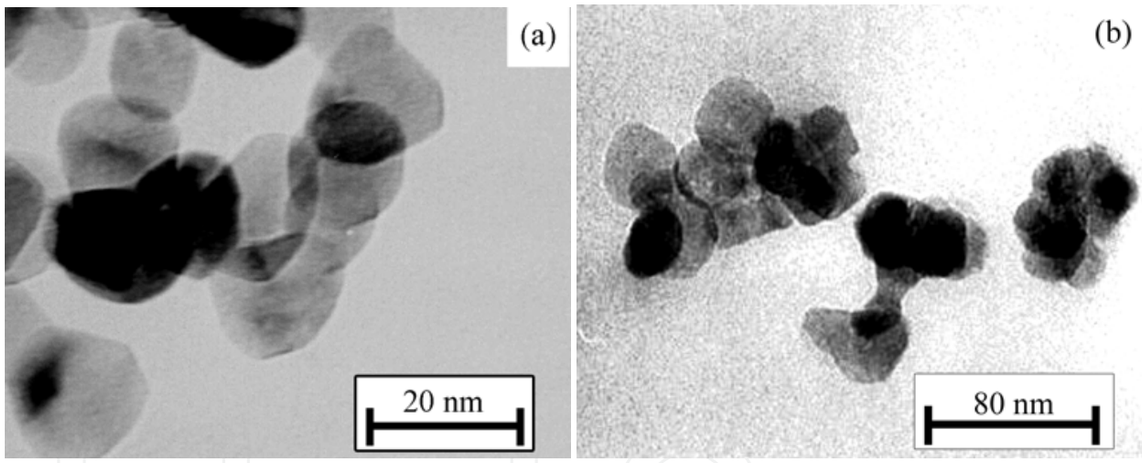

Fig. 30. TEM images of a) core and b) core/shell nanoparticles.

Optical absorptions of the obtained nanoparticles are shown in Fig. 32. Absorption coefficient, *a(λ)*, for allowed direct transition of semiconductors is given by the following expression:

$$\alpha = A\frac{\left(h\nu - E_g\right)^n}{h\nu} \tag{11}$$

where A is coefficient of the given electronic transition probability, E_g is band gap energy and n is equal to 0.5 and 2 for allowed direct and indirect transitions and 1.5 and 3 in case of forbidden direct and indirect transitions, respectively. In current study, the best fit of $\left(\alpha h\upsilon\right)^{1/n}$ versus photon energy was obtained 0.5 for both of core and core/shell.

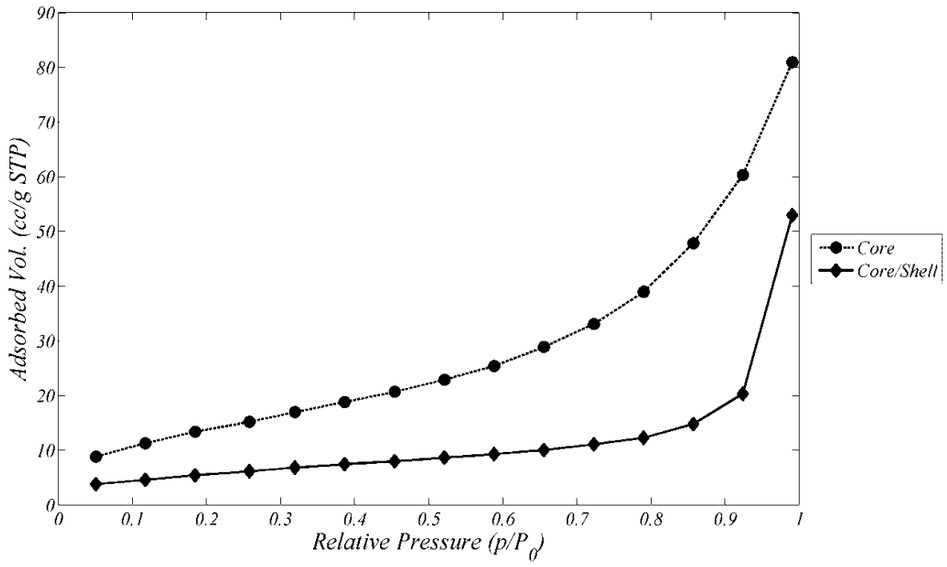

Fig. 31. BET adsorption isotherms.

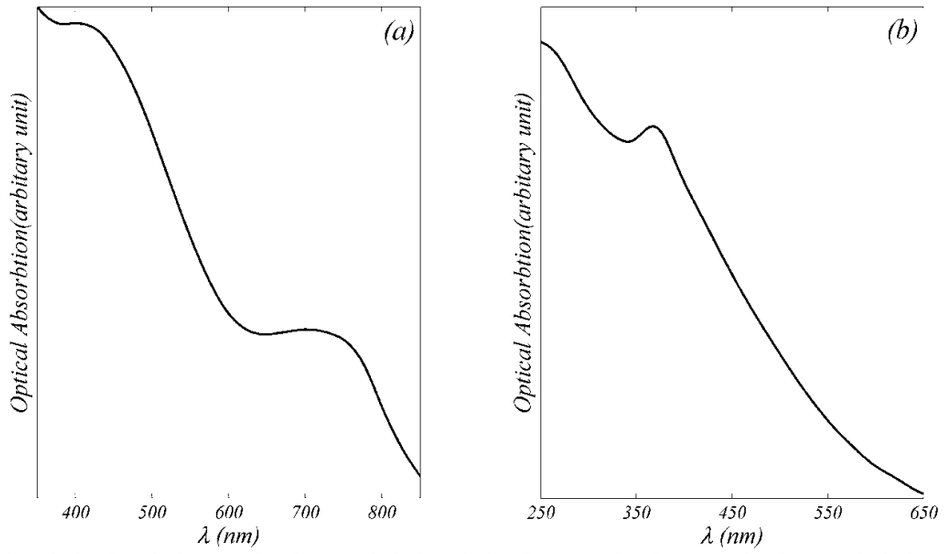

Fig. 32. UV-Vis spectra of a) core and b) core/shell nanoparticles.

Fig. 33 shows plots of $(\alpha h\upsilon)^{1/n}$ versus photon energy for both core and core/shell nanoparticles. As can be seen from these plots, in core (Fig. 33a) there are two regions in optical absorption. First one with 1.89 ev energy is related to nature of spinel structure of Co_3O_4. In spinel structure of Co_3O_4, Co(III) ions locate in center of structure. This fact affects the band structure and thus, gives rise to a sub- band in the bandgap energies. Thus two bands could be detected in absorptions, first related to excitation of O(II)→Co(III) which results in emerging 2nd band gap energy in 1.4 ev. This gap should be located inside of band gap and thus the bandgap should have larger amounts. 1.89 ev is the real optical band gap of Co_3O_4. The band gap shows a reduction in comparison with bulk Co_3O_4, there are many

reports in which main reason for red shift in nano Co_3O_4 was contributed to quantum-confinement effects.

The optical properties of Core/shell are somehow different from core itself (Fig. 33b). As could be seen in Fig. 6, the obtained band gap is 3.42 ev which shows a blue shift in comparison with bulk ZnO (E_g^{bulk} =*3.3ev*). In our previous work, we reported red shift in ZnO band gap (E_g=*3.27 ev*) prepared by same way. This blue shift could be resulted from two phenomena: first, in large band gap semiconductors, mainly, a reduction in size results in an extension in band gaps. As shown in TEM images some parts of ZnO shells in nanocomposite are thinner than 25nm which could make a blue shift. Also, Existence of exciton shoulder in absorption spectra of nanocomposite is another claim for making ZnO with thicknesses low enough for emerging exciton shoulder at room temperature. Second, existence of p-type Co_3O_4 in core adjacent to n-type ZnO affect the final properties of nanocomposite and make a blue shift in final optical band gap of nanocomposite.

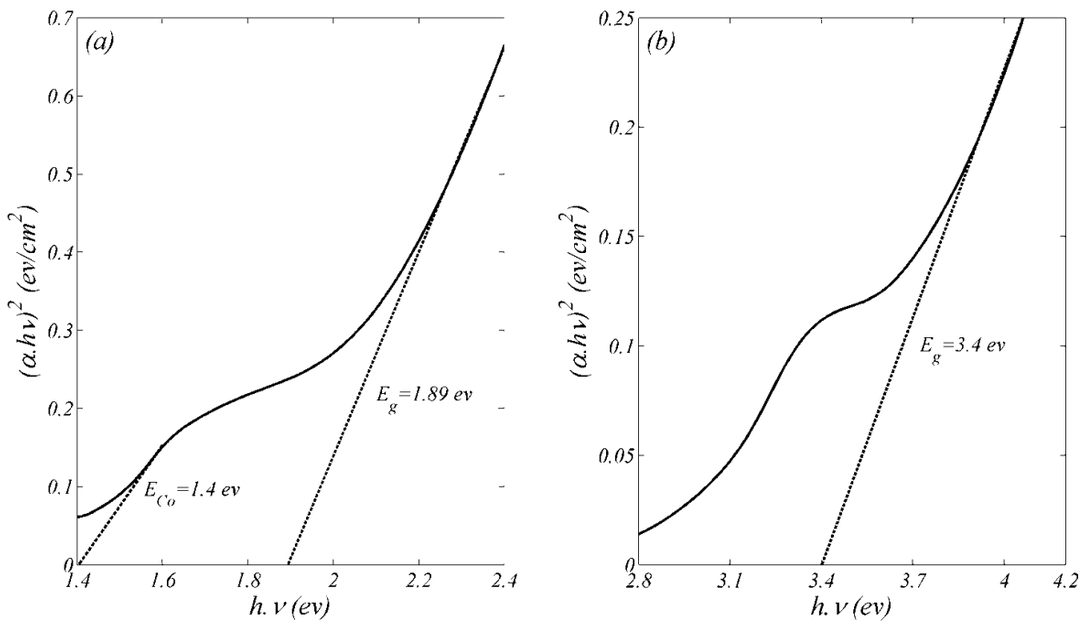

Fig. 33. $(\alpha h\upsilon)^{1/n}$ vs. photon energy for obtained a) Co_3O_4 and b) Co_3O_4/ZnO.

Fig. 34 shows magnetic behaviours of Co_3O_4 and Co_3O_4/ZnO core/shells. Also, in Table 11 the magnetic properties of prepared materials are listed. Co_3O_4 due to its spinel structure shows anti-ferromagnetic characteristics, however, the core shows dilute ferromagnetic characteristic. This might be due to existence of oxygen in spinel structure of Co_3O_4 which avoids direct interaction of magnetic momentums.

As could be seen from Table 11, the amount of saturation magnetism in core/shell nanocomposites shows a decrease in comparison with core. In core/shell Co_3O_4/ZnO nanocomposites there are two phenomena. ZnO is a diamagnetic material. These materials in VSM analysis show a negative magnetization and no hysteresis loop. ZnO can change its magnetic characteristic by doping of some impurities such as Co, Mn, Ni, etc. These dilute dopants can change the diamagnetic behaviour of ZnO into carrier induced ferromagnetic

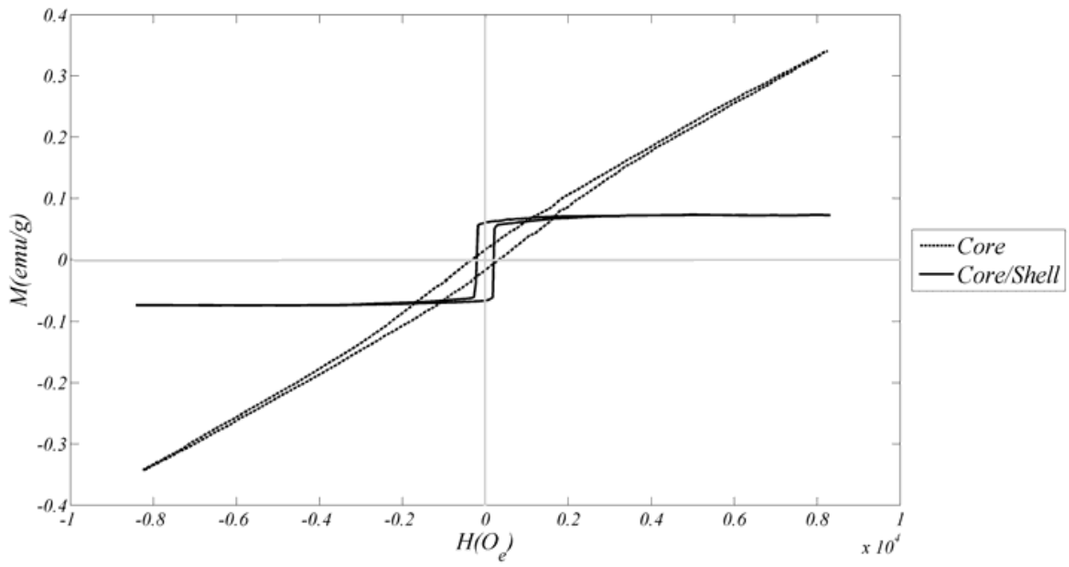

Fig. 34. VSM spectra of a) core and b) core/shell nanoparticles.

Sample	M_S(emu/g)	H_C(Oe)
Core	0.34	325
Core/shell	0.08	222

Table 11. Magnetic properties of core and core/shell.

materials. Existence of Co_3O_4 core adjacent to ZnO films results in a dilute ferromagnetic characteristic due to ability in ordering disorder spins arrays in surface of Co_3O_4 which in magnetic field could be ordered and compensation diamagnetic characteristic of shell component. On the other hand, by applying a diamagnetic shell on a magnetic material, saturation magnetism of core decreases. This decrease could be intensified by thickening of diamagnetic shell.

5. References

[1] Haga K., Ishii T., Mashiyama J., Ikeda T., Japanese Journal of Applied Physics 31 (1992) 3156.
[2] Kim H.T., Byun J.D., Kim Y., Materials Research Bulletin 33 (1998) 963.
[3] Kim H.T., Kim S.H., Nahm S., Byun J.D., Journal of the American Ceramic Society 82 (1999) 3043.
[4] Dulin F.H., Rase D.E., Journal of the American Ceramic Society 43 (1960) 125.
[5] Chang Y.S., Chang Y.H., Chen I.G., Chen G.J., Chai Y.L., Wu S., Fang T. H., Journal of Alloys and Compounds 354 (2003) 303.
[6] Kim H.T., Nahm S., Byun J.D., Kim Y., Journal of the American Ceramic Society 82 (1999) 3476.

[7] Golovchanski A., Kim H.T., Kim Y.H., Journal of the Korean Physical Society 32 (1998) S1167.
[8] Sohn J.H., Inaguma Y., Yoon S.O., Itoh M., Nakamura T., Yoon S. J., Kim H. J., Japanese Journal of Applied Physics 33 (1994) 5466.
[9] Li C.F., Bando Y., Nakamura M., Kimizuka N., Kito H., Mater. Res.Bull. 35 (2000) 351.
[10] Zakrzewska K., Thin Solid Films, 391 (2001) 229.
[11] Esmaielzadeh Kandjani A., Farzalipour Tabriz M., Pourabbas B., Mater. Res. Bull., 43 (2008), 645.
[12] M.R. Vaezi, S. K. Sadrnezhaad, A. Esmaielzadeh Kandjani, L. Nikzad, N.A. Arefian, S. Alibeigi, M. Farzalipour Tabriz, S.H. Mir Shah Ghassemi, J. Samei, Materials Science Poland, 25, No. 4, 2007, 1109- 1117.
[13] Haro-poniatowski E., Ostuski H., Sada E., J. Mater. Res., 9 (1994) 2102.
[14] Tang Z., Zhang J., cheng Z., Zhang Z., Journal of materials chemistry and physics 77 (2002) 314.
[15] Cuna W., Jincai Z., Xinming W., Bixian M., Guoying S., Pingan P., Jiamo F., Appl. Catal. B-Environ., 39 (2002), 269.
[16] Zhang M., An T., Hu X., Wang C., Sheng G., Fu J., Appl. Catal. A-Gen., 260 (2004) 215.
[17] Bandara J., Tennakone K., Jayatilaka P.P.B., Chemosphere, 49 (2002), 439.
[18] Wen Z., Wang G., Lu W., Wang Q., Zhang Q., Li J., Cryst. Growth. Des., 7 (2007), 1722.
[19] B.P.J. de Lacy Costello, Ewen R.J., Guernion N., Ratcliffe N.M., Sensor. Actuat. B-Chem., 87 (2002), 207.
[20] Sun S., Meng G., Zhang G., Zhang L., Cryst. Growth. Des., 7 (2007), 1988.
[21] Bagheri-Mohagheghi M. M., Shokooh-Saremi M., Thin Solid Films, 441 (2003), 238.
[22] Jiang J.C., Lian K., Meletis E. I., Thin Solid Films, 411 (2002), 203.
[23] Mukashev B. N., Tokmoldin S.Zh., Beisenkhanov N.B., Kikkarin S.M., Valitova I.V., Glazman V.B., Aimagambetov A.B., Dmitrieva E.A., Veremenithev B.M., Mat. Sci. Eng. B, 118 (2005), 164.
[24] Lorrain N., Chaffron L., Carry C., Delcroix P., Caër G. L., Mat. Sci. Eng. A, 367 (2004), 1.
[25] Pires F.I., Joanni E., Savu R., Zaghete M.A., Longo E., Varela J.A., Mater. Lett., 62 (2008), 239.
[26] Wu D. S., Han C. Y., Wang S. Y., Wu N. L., Rusakova I. A., Mater. Lett., 53(2002), 155.
[27] Jia Z. j., Zhu L. p., Liao G. h., Yu Y., Tang Y. W., Solid State Commun., 132 (2004), 79.
[28] Kobayashi T., Kimura Y., Suzuki H., Sato T., Tanigaki T., Saito Y., Kaito C., J. Cryst. Growth, 243 (2002), 143.
[29] Chouvin J., Branci C., Sarradin J., Fourcade J. O., Jumas J. C., Simon B., Biensan Ph., J. Power Sources, 81–82 (1999), 277.
[30] Culity B.D., *Elements of X-ray diffraction*, Addison-Wesley Company, USA, 1978.
[31] X. Zhong, R. Xie, Y. Zhang, T. Basche´ , W. Knoll, Chem. Mater., 17 (2005) 4038.
[32] Wu C., Qiao X., Chen J., Wang H., Tan F., Li S., Mater. Lett., 60 (2006), 1828.
[33] Zakrzewska K., Thin Solid Films, 391(2001), 229.
[34] M. Ando, T. Kobayashi, S. Iijima, et al. J. Mat. Chem. 7, 1779-1783, (1997)
[35] F. A. Cotton, G. Wilkinson, Advanced Inorganic Chemistry, Wiley, Newyork, 1972
[36] P. Cossee, Rec. Trav. Chim. Pays-bas 75 (1956) 1089

[37] L. Armelao, D. Barreca, S.Gross, A.Martucci, M.Tieto, E.Yondella, Journal of Non-Crystalline solids 293-295 (2001) 477-482
[38] C. H. kwon, H. K. Hong, D. H. Yun, K. Lee, S. T. Kim, Y. H. Roh, B. H. Lee, Sens. Actuators B, 24-25,610-613, (1995)
[39] G. Behr, W. Fhegel, Sens. Actuators B, 33-37, 2627-2632, (1995)
[40] C. Garzella, E. Comini, E. Tempesti, C. Frigeri, G. Sberveglieri, Sens. Actuators B, B 68 189–196, (2000)
[41] N. Barsan, M. Schweizer Berberich, W. Gopel, J. Anal. Chem., 365, 287-304, (1999)
[42] T.Seiyama, H. Futata, F. Era, N. Yamazoe, Mater. Sci. , 8 , 63-65, (1972)
[43] N. Xinshu, D. Weiping, D. Weimin, Sensors and actuators B 99(2004) 405-409
[44] X. Zhou, Y. Kobayashi, V. Romanyuk, N. Ochuchi, M. Takeda, S. Tsunekawa, A. Kasuya, Appl. Surf. Sci., 242 (2005) 281.
[45] Z. W. Zhao, Z. P. Guo, H. K. Liu, J. Power Sources, 147(2005) 264- 268.
[46] L. Wu, Y. Wu, X. pan, F. Kong, Opt. Mater. 28 (2006) 418-422.
[47] A. Shokuhfar, J. Samei, A. Esmaielzadeh Kandjani, M.R. Vaezi, Deffect Diffus. Forum, 273-276 (2008) 626-631.
[48] F. Pertlik, Monatsh. Chem. 130, (1999), 1083-1088.
[49] J.D.H. Donnay, D. Harker, Amer. Mineral. 22 (1937) 446.
[50] P. Hartman, W.G. Perdok, Acta Crystallogr. 8 (1955) 525.
[51] W.-Z. Zhong, G.-Z. Liu, Sci. China (B) 24 (4) (1994) 394.
[52] J. Du, Z. Liu, Y. Huang, Y. Gao, B. Han, W. Li, G. Yang, J. Cryst. Growth 280 (2005) 126–134.
[53] Y.H. Ni, X.W. Wei, X. Ma, J.M. Hong, J. Cryst. Growth 283 (2005) 48–56.
[54] G. Sun, M. Cao, Y. Wang, C. Hu, Y. Liu, L. Ren, Z. Pu, Mater.Lett. 60 (2006) 2777–2782.
[55] Z. Li, Y. Xiong, Y. Xie, Nanotechnology 16 (2005) 2303–2308.
[56] D. J. Shaw, Introduction to Colloid and Surface Chemistry, Butterworth-Heinemann, Oxford, 1992.
[57] R. Atkins, V.S.J. Craig, E.J. Wanless, S. Biggs, Adv. Colloid Interfac. 103 (2003) 219–304.
[58] W.J. Li, E.W. Shi, W.Z. Zhong, Z.W. Yin, J. Cryst. Growth 203 (1999) 186-196.
[59] W.Z. Zhong, D.Y. Tang, J. Cryst. Growth 166 (1996) 91.
[60] W.Z. Zhong, X.L. Yu, Sci. China Ser. E 41 (4) (1998).
[61] Y. Vronko, K. Gorbachev, V.V. Osiko, ICCG-10 Poster, B 34 (1992) 57.
[62] H. Kouta, Y. Kuwano, K. Ito, F. Marumo, J. Cryst. Growth 114 (1991) 676.
[63] Y. Wang, L. Sun, L.G. Kong, J.F. Kang, X. Zhang, R.Q. Han, J. Alloy Compd. 423 (2006) 256–259.
[64] B. Basavalingu, J. A. K. Tareen, G. T. Bhandage, J. Mater. Sci. Lett. 5 (1986) 1227-1229.
[65] I. N. Smallwood, Handbook of organic solvent properties, John-Wiley & Sons Inc., New york,1996.
[66] Y. Lu, Y.D. Yin, Z.Y. Li, Y.N. Xia, Nano Lett. 2, 785, (2002).
[67] N. Yu, X.P. Hao, X.G. Xu, M.H. Jiang, Mater. Lett. 61, 523, (2007).
[68] W.Z. Lin, L. Yi, Z. Ze, Handbook of nanophase and Nanostructured Materials, (Plenum, Kluwer Academic 2002).
[69] M.C. Hidalgo, M. Aguilar, M. Maicu, J.A. Navío, G. Colón, Catalysis Today. 129, 50, (2007

[70] M.R. Vaezi, Mater. Chem. Phys. 110, 89, (2008).
[71] N.V. Duy, N. V. Hieu, P. T. Huy, N. D. Chien, M. Thamilselvan, J. Yi, Physica E. 41, 258, (2008).

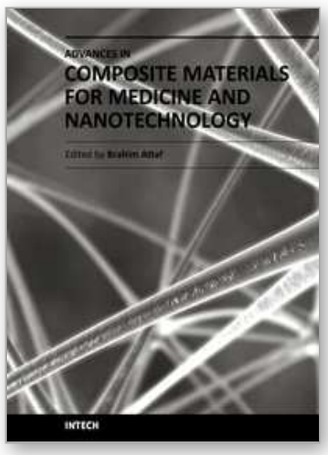

Advances in Composite Materials for Medicine and Nanotechnology

Edited by Dr. Brahim Attaf

ISBN 978-953-307-235-7
Hard cover, 648 pages
Publisher InTech
Published online 01, April, 2011
Published in print edition April, 2011

Due to their good mechanical characteristics in terms of stiffness and strength coupled with mass-saving advantage and other attractive physico-chemical properties, composite materials are successfully used in medicine and nanotechnology fields. To this end, the chapters composing the book have been divided into the following sections: medicine, dental and pharmaceutical applications; nanocomposites for energy efficiency; characterization and fabrication, all of which provide an invaluable overview of this fascinating subject area. The book presents, in addition, some studies carried out in orthopedic and stomatological applications and others aiming to design and produce new devices using the latest advances in nanotechnology. This wide variety of theoretical, numerical and experimental results can help specialists involved in these disciplines to enhance competitiveness and innovation.

How to reference

In order to correctly reference this scholarly work, feel free to copy and paste the following:

Mohammad Reza Vaezi (2011). Coupled Semiconductor Metal Oxide Nanocomposites: Types, Synthesis Conditions and Properties, Advances in Composite Materials for Medicine and Nanotechnology, Dr. Brahim Attaf (Ed.), ISBN: 978-953-307-235-7, InTech, Available from: http://www.intechopen.com/books/advances-in-composite-materials-for-medicine-and-nanotechnology/coupled-semiconductor-metal-oxide-nanocomposites-types-synthesis-conditions-and-properties

INTECH
open science | open minds

InTech Europe
University Campus STeP Ri
Slavka Krautzeka 83/A
51000 Rijeka, Croatia
Phone: +385 (51) 770 447
Fax: +385 (51) 686 166
www.intechopen.com

InTech China
Unit 405, Office Block, Hotel Equatorial Shanghai
No.65, Yan An Road (West), Shanghai, 200040, China
中国上海市延安西路65号上海国际贵都大饭店办公楼405单元
Phone: +86-21-62489820
Fax: +86-21-62489821

IntechOpen